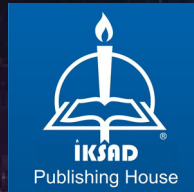


# **NEW APPLICATIONS IN BASIC SCIENCES**

**EDITOR**  
**Murat KIRANŞAN**

**AUTHORS**  
**Adem YOLCU**  
**Adnan KILIÇ**  
**Muhammed Faruk YILDIRIM**  
**Kadir Can ERBAŞ**  
**Taha Yasin ÖZTÜRK**  
**Tuba ÖZDEMİR ÖGE**



# **NEW APPLICATIONS IN BASIC SCIENCES**

## **EDITOR**

Murat KIRANŐAN

## **AUTHORS**

Adem YOLCU

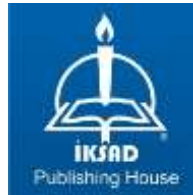
Adnan KILIŐ

Muhammed Faruk YILDIRIM

Kadir Can ERBAŐ

Taha Yasin ÖZTÖRK

Tuba ÖZDEMİR ÖGE



Copyright © 2021 by iksad publishing house  
All rights reserved. No part of this publication may be reproduced,  
distributed or transmitted in any form or by  
any means, including photocopying, recording or other electronic or  
mechanical methods, without the prior written permission of the publisher,  
except in the case of  
brief quotations embodied in critical reviews and certain other  
noncommercial uses permitted by copyright law. Institution of Economic  
Development and Social  
Researches Publications®  
(The Licence Number of Publisher: 2014/31220)  
TURKEY TR: +90 342 606 06 75  
USA: +1 631 685 0 853  
E mail: iksadyayinevi@gmail.com  
www.iksadyayinevi.com

It is responsibility of the author to abide by the publishing ethics rules.  
Iksad Publications – 2022©

**ISBN: 978-625-8213-11-9**  
Cover Design: İbrahim KAYA  
August / 2022  
Ankara / Turkey  
Size = 16x24 cm

## **CONTENTS**

### **PREFACE**

*Assist. Prof. Murat KIRANŞAN*.....1

### **CHAPTER 1**

#### **AN ARDUINO-BASED MULTI-PURPOSE ENVIRONMENTAL MEASUREMENT DEVICE**

*Assoc. Prof. Dr. Tuba ÖZDEMİR ÖGE*.....3

### **CHAPTER 2**

#### **INVESTIGATION OF APSIDAL MOTION OF DETACHED SYSTEMS RW LAC AND TV CET**

*Dr. Muhammed Faruk YILDIRIM* .....25

### **CHAPTER 3**

#### **SURFACE AREA OF SUPERELLIPSOIDS AND ITS APPLICATION TO PHYSICS PROBLEMS**

*Dr. Kadir Can ERBAŞ* .....39

### **CHAPTER 4**

#### **GEANT4 SIMULATION OF THE EFFECT OF TRAPEZOIDAL AND RECTANGULAR CRYSTAL SHAPES ON THE TRANSMISSION OF LYSO: Ce EMISSION PHOTONS**

*Assist. Prof. Adnan KILIÇ* .....65

### **CHAPTER 5**

#### **FUZZY PARAMETERIZED INTUITIONISTIC FUZZY SOFT TOPOLOGY AND ITS APPLICATION TO DECISION-MAKING**

*Asst. Prof. Adem YOLCU*

*Assoc. Prof. Taha Yasin ÖZTÜRK* .....85



## **PREFACE**

It is our honor to present information on physics, physics engineering and mathematics studies. We are happy to contribute to international scientific studies. This book was first published and presented in chapters. The prepared book consists of five chapters explaining new and current issues. It is a professional book with important methods and applications in physics, physics engineering and mathematics.

This study contains very valuable studies by Assoc. Prof. Dr. Tuba Ozdemir Oge (An Arduino-Based Multi-Purpose Environmental Measurement Device); Dr. Muhammed Faruk Yildirim (Investigation of apsidal motion of detached systems rw lac and tv cet); Dr. Kadir Can Erbas (Surface area of superellipsoids and its application to physics problems); Assist. Prof. Dr. Adnan Kilic (Geant4 Simulation of the Effect of Trapezoidal and Rectangular Crystal Shapes on the Transmission of Lyso: Ce Emission Photons); Assist. Prof. Dr. Adem Yolcu, Assoc. Prof. Dr. Taha Yasin Ozturk (Fuzzy parameterized intuitionistic fuzzy soft topology and its application to decision-making). We would like to thank the managers and employees of IKSAD.

**Assist. Prof. Dr. Murat KIRANŞAN**  
**University of Gumushane**  
**Editor**



**CHAPTER 1**  
**AN ARDUINO-BASED MULTI-PURPOSE ENVIRONMENTAL**  
**MEASUREMENT DEVICE**

Assoc. Prof. Dr. Tuba ÖZDEMİR ÖGE<sup>1</sup>

---

<sup>1</sup>Bartın University, Vocational School of Health Services, Department of Medical Services and Techniques, Opticianry Program, Bartın, Turkey. E-mail: [tozdemir@bartin.edu.tr](mailto:tozdemir@bartin.edu.tr), ORCID ID, <https://orcid.org/0000-0001-6690-7199>.



## INTRODUCTION

Micro-controllers constitute the basis of embedded systems in all smart systems that are widely used today (Akar, 2018), and they have been frequently used in many fields, particularly in electronic projects and studies along with actuators and sensors. Microcontrollers consist of a CPU (Central Processing Unit), RAM (Random Access Memory) and ROM (Read Only Memory) units, I/O (Input/Output) ports, serial and parallel ports, counters, and A/D (Analog/Digital) and D/A (Digital / Analog) converters in their structure. The structure of these integrated circuits consists of internal connections, transistors, diodes, capacitors, and resistors which are combined on a silicon crystal. Semiconductor crystals and silicon transistors are used in the production of electronic circuit elements such as diodes and integrated circuits (Özdemir, 2011). Open-source development platforms such as Arduino provide ease of use due to several features gathered in a single open-source hardware, and they have become indispensable tools for electronic studies (Dipova, 2017). Arduino Integrated Development Environment (IDE) software (<https://www.arduino.cc/en/software>) is used for programming the micro-controller integrated into the Arduino (Dökmetaş, 2016) platform. The Arduino platform involves the use of Atmel series micro-controllers, analog and digital input-output (I-O) pins, USB input as well as supply and reset circuits. By use of this platform, several advanced technology applications can be easily performed with a variety of compatible auxiliary components and sensors (Çobanoğlu, 2017). The Arduino platform has found a wide usage around the world particularly in the field of education and prototyping as a result of its user-friendly interface and commercial availability of a wide range of Arduino-compatible peripheral and auxiliary units. Open-source electronic prototyping platforms such as Arduino are expected to draw more interest in the near future where digitalization of almost all industrial fields through Industry 4.0 and its constituents such as augmented reality, additive manufacturing, internet

of things and other key technologies and concepts will be partly dependent on the utilization of these technologies by a larger number of people. Some of the studies that have drawn on this open-source platform are as follows. In their study on international collaborative student projects performed on digital electronic media using open-source tools, Rodriguez-Sanchez et al. (2020), stated that the use of open-source development tools enabled the students to have better learning experience with a higher motivation. (Rodriguez-Sanchez et al., 2020). Mohammad M. Abdellatif and Walaa Mohamed (2020) developed and introduced a remote-controlled health-care system named "Telemedicine" on the Internet of Medical Things (IoMT) platform to establish a remote connection between doctors and patients (Abdellatif and Mohamed, 2020). Daigavane and Gaikwad (2017) introduced an IoT based water quality monitoring system for real time measurement of the physical and chemical parameters of drinking water supplies (Daigavane and Gaikwad, 2017). Ozdemir Oge (2018) developed an Arduino-based automatic irrigation system using soil-moisture and temperature sensors. In this study, an efficient irrigation system was developed to measure the moisture content of the soil and to adjust the irrigation amount accordingly (Özdemir Öge, 2018). Ersin (2015) developed a solar-powered automated irrigation system using an Arduino platform. In this system, the optimum amount of water was determined by use of an Arduino Uno platform (Ersin, 2015). Elverir (2019) developed a portable laboratory platform to perform real time measurement of the temperature, pH and turbidity values of water samples by use of an Arduino platform. In this work, the measurement sensitivity of the sensors was determined by testing the mentioned physical properties of samples with predefined temperature, turbidity, and pH values (Elverir, 2019). Järvinen et al. (2017) performed the design and testing process for a cyber-physical indoor-outdoor gas sensing system that was capable of versatile gas detection. They used a well-established Arduino microcontroller and a Raspberry Pi single

board computer and realized the functionality of the system with C and Python programming languages (Järvinen et al., 2017). Bahir (2016) developed a remote-controlled smart home automation system that monitors and controls the temperature, humidity, gas leak, fire, movement, and rain amount in a house (Bahir, 2016). Ekmekçi (2017) developed a mobile system with a graphic display to monitor and interpret the electrocardiogram (ECG), electromyogram (EMG) and pulse oxymetry (SpO<sub>2</sub>) values of patients received from an e-Health sensor platform kit for remote health monitoring purposes (Ekmekçi, 2017). Karami et al. (2018) developed and introduced a reliable and robust Arduino-based data gathering system indoor environmental quality (IEQ) monitoring purposes. Their toolbox was capable of performing temperature, relative humidity, occupancy etc. measurements through the use of a ZigBee communication protocol, Arduino boards, and an XBee receiver (Karami et al., 2018). In a more recent work, Netto and Arigony-Neto (2019) designed and explained a low-cost toolbox customized to determine the characteristics of glacial environments in an attempt to identify climate changes and weather patterns. Their low-cost solution involved the use of open-source software and hardware platforms (Netto and Arigony-Neto, 2019).

Potentiometric glass electrodes, ion-sensitive field effect transistors (ISFETs), metal-metal oxide transistors, indium-tin-oxide based (ITO-based) electric double layer (EDL) and thin-film-transistor (TFT) pH detectors are used in electrochemical measurements whereas optical measurements involve the use of chemical indicators such as litmus paper, fluorescent pH probe and optical fiber measurement probes (Ntella, 2017). Various pH-sensor based applications have been proposed in the literature. Qian et al. introduced a safe, efficient, and reliable pH sensor signal receiving and monitoring system design (Qian et al., 2017). Mashud et al. (2011) designed a microcontroller based digital pH meter. Their system design comprises of a low voltage

power supply, a sensor circuit, a buffer amplifier, a micro-controller unit and a display circuit (Mashud et al., 2011).

It is also important to measure the pH value of foods as it has direct impact on food quality and safety. pH meters are widely used in the pharmaceutical industry as well. In addition, pH meters are used to check the parameters of water and water properties. Similarly, various devices are used in the industrial field where physical and chemical properties are tested and measured with precision. The current study likewise aims to introduce the design and development stages of a multi-purpose low cost environmental measurement and monitoring toolkit that is capable of simultaneous real time measurement of environmental parameters such as water and air temperature, humidity, pH and water turbidity parameters in a single toolbox by use of a pH sensor connected to a BNC (Bayonet Neill–Concelman) connector, a liquid temperature sensor (DS18B20), temperature and humidity sensors (DHT22) and a turbidity sensor. The current study is distinguished from the others as it uses a single Arduino-Mega platform to perform such a variety of tasks, thus reducing the component cost. The pH interface is programmed after being plugged into the analog input port of the Arduino controller. Apart from the pH measurement, the device performs real-time measurement of the temperature of the environment as well as the temperature and turbidity of the subject liquid. The data obtained from the sensors were transferred to the serial monitor and LCD screen which were compared with the test results of commercial measurement device (for temperature measurement) and test kits (for pH measurement). The proposed device is distinguished from similar works by simultaneous measurement of the parameters of two different media (water and air) by use of a single microprocessor on an IoT compatible structure.

## MATERIAL AND METHODS

Sensors are used to convert signals from a specific energy domain into electrical signals. The signals received by sensors are processed by microprocessors or microcontrollers for their further processing into useful information. In this section, brief information is given about the sensors and the materials used and the design of the subject device. The proposed experimental-setup consists of an Arduino Mega board, an air temperature and humidity sensor, temperature sensors, a liquid turbidity sensor and a pH sensor with BNC (Bayonet Neill – Concelman) connector. In addition, power supplies, resistors, strain gauges, experimental circuit boards and jumper cables were used as electronic auxiliary units. As shown in Figure 1, Arduino Mega 2560 has input and output pins and it can be powered by a battery, an adapter, a charger, and a computer USB port, which largely contributes to its versatility and functionality in prototyping studies.

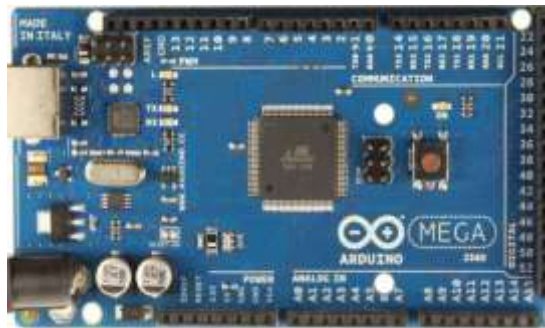


**Figure 1.** Arduino MEGA

Micro-controllers are among the important technological devices used in the development of smart domestic and industrial projects, robot technologies and various industrial devices. Arduino Mega 2560 is an Atmega2560 based micro-controller board and has 256 KB of memory. It has 54 digital input/output pins, and these pins can be used as both input and output. It has 16 analog inputs and 4 UART (hardware serial port), 16 Mhz crystal, usb socket, power

socket, ICSP connector and reset button. 8 pins are used for receiver (RX) and transmitter (TX) purposes used in TTL serial data communication. Also, 15 pins provide 8-bit PWM (pulse width modulation) output. SPI (50, 51, 52, 53) pins are the pins that provide SPI communication using the SPI library. It has 16 analog inputs from A0 to A15 (Çobanoğlu, 2017).

Portable pH meters are one of the important electronic devices used to measure the pH value quickly and effectively in various laboratories, primarily in industrial areas.  $5 \pm 0.2$  V (AC - DC) heating voltage (voltage), 5 -10 mA operating current, pH 0-14 detectable concentration range, 0-80 °C detection temperature range, response time  $\leq 5$  sec, setting time  $\leq 60$  sec, device operating power  $\leq 0.5$  W, operating temperature -10 ~ 50 °C, 95 % RH humidity (nominal humidity 65% RH), 42 mm  $\times$  32 mm  $\times$  20 mm module size and pH 0-14 detection regulator are among the features of the pH sensor module used in the current study as shown in Figure 2 (a). A pH meter measured on a scale of 0-14 consists of an analog or digital indicator. In the pH sensor, electrodes are immersed in the solution. Electrodes measure the conductivity of the liquid and the resulting voltage difference is converted to the pH value that is a unit of measure describing the degree of acidity or alkalinity of a solution.

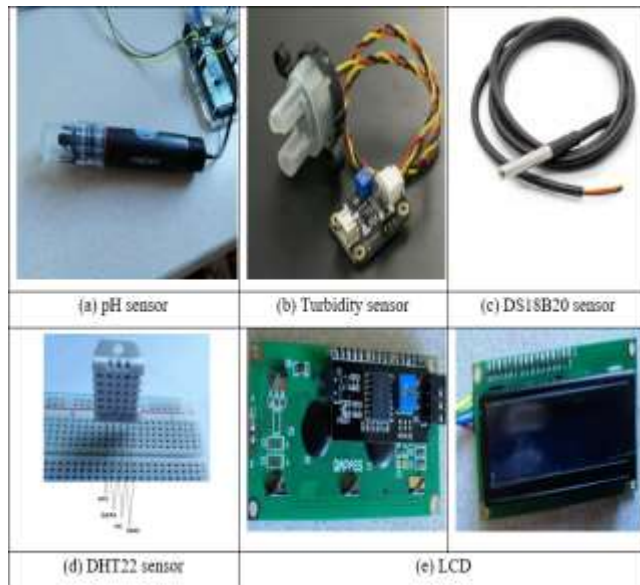


**Figure 2.** Sensors

Turbidity is the measurement of water clarity and water quality. The turbidity detector detects the water quality by measuring the turbidity level. Suspended sediments such as clay, soil and silt particles enter the water and affect the water quality. Suspended sediments may contain contaminants such as phosphorus, pesticides, or heavy metals. The light is used to detect particles suspended in water by measuring the amount of light transmittance and scattering that varies with the total amount of suspended solids (TSS) in water. Suspended particles reduce the depth of light penetration into the water, thus increasing the turbidity of the water. Turbidity level increases with increasing TSS (total suspended solids) value. Turbidity sensors are used in water quality in rivers and streams, wastewater and wastewater measurements, settlement control tools of ponds, sediment transport studies and laboratory measurements (Fondriest Environmental Learning Center, 2021). Turbidity sensor provides analog and digital signal output types. Threshold value can be set in digital signal type (DF ROBOT, 2020). The turbidity sensor has 5V DC operating voltage,

30 mA (MAX) current, -30 °C to 80°C operating temperature. The measuring range of the sensor is: 0 ~ 1000 NTU as shown in Figure 2 (b). Turbidity measurement was achieved by detecting the quality of the water with the water turbidity sensor. It is connected analogously to the circuit.

The liquid temperature sensor (DS18B20) is a digital waterproof sensor used to measure the temperature of the liquid in this study. Its working principle is detection of temperature rise by monitoring the voltage variation between the transistor terminals in the diode. The sensor has 3.0 V-5.0 V operating voltage, -10 °C-80 °C temperature reading (with  $\pm 0.5$  °C precision), 9 or 12 bit resolution, communication with 1-wire interface, low response time (<750 mS) as shown in Figure 2 (c). DS18B20 Digital Temperature Sensor, 4.7k resistor and jumper cables were used on digital pins and connections were made on the experimental circuit. OneWire library (`#include <OneWire.h>`) was added in the program.

DHT22 humidity and temperature sensor was used to measure the humidity and temperature values in the ambient air. DHT22 sensor and pin outs are shown in Figure 2 (d). The humidity range of this sensor is 0-100 %, the temperature range is -40 °C - 123.8 °C and the supply voltage varies between 3 V-5 V.

The usage of serial I2C 16x2 character LCD module is explained in Figure 2 (e). `#include <LiquidCrystal_I2C.h>` // I2C and `#include <Wire.h>`//Wire.h libraries have been added. LCD screen properties are defined as `LiquidCrystal_I2C LCD (0x27, 16, 2)`.

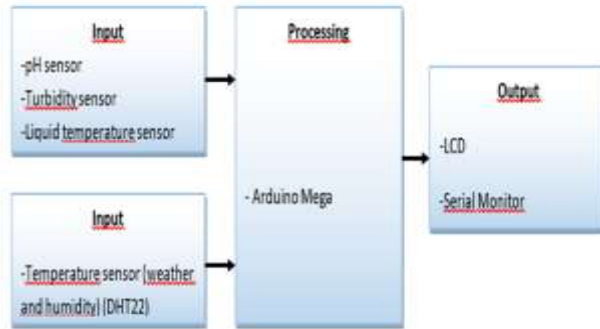


**Figure 3.** Flow diagram

pH meter is connected to Arduino via analog and digital pin. The software prepared on the micro-controller was recorded by entering the sensor libraries on the program to be created on the Arduino software platform. The workflow process of the study is given in Figure 3 and the connections of the sensors are illustrated in Figure 4.

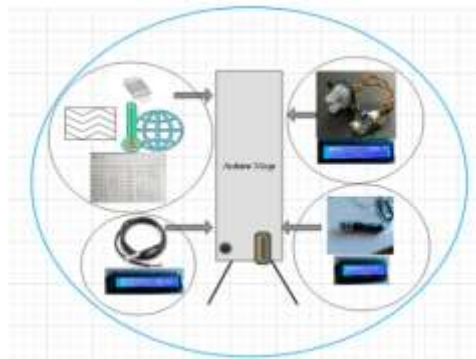


**Figure 4.** The connection of sensors

The number and variety of communication ports on Arduino Mega (Serial1, Serial2, Serial3 ports) provides enhanced functionality in prototyping projects (Sevinç, 2015). In addition to the mentioned functionalities of these platforms, embedded micro-controllers provide great advantage due to the integration of CPU, RAM and I/O on a single chipset along with the data bus that enables the data transfer between these units (Akar, 2018) which provide the researcher with the

advantage to focus only on the system design by minimizing the number of electronic design components to be dealt with.

### RESEARCH FINDINGS

Electronic projects maintain their importance today along with the rise of smart systems. The use of smart systems involves a wide range of applications and concepts including e-health, home automation, control systems, security, artificial intelligence, machine learning, robotic coding, internet of things, smart applications (smart city, smart environment, smart water, smart agriculture, smart husbandry, smart energy, smart cities, smart metering, smart shopping, smart logistics, etc.). In line with the integration of smart systems and their components into every aspect of our lives, several works and projects have been carried out on use of open-source hardware and corresponding software such as Arduino sensors with Arduino IDE for replacement of commercially available water and ambient air quality monitoring systems with cost-effective products.

pH sensor has a simple, convenient, and practical connection, making it very suitable for online monitoring. The pH sensor was connected to the BNC connector, then the PH2.0 interface was plugged into the analog input port of the Arduino Mega 2560 controller. After programming, pH values were obtained.

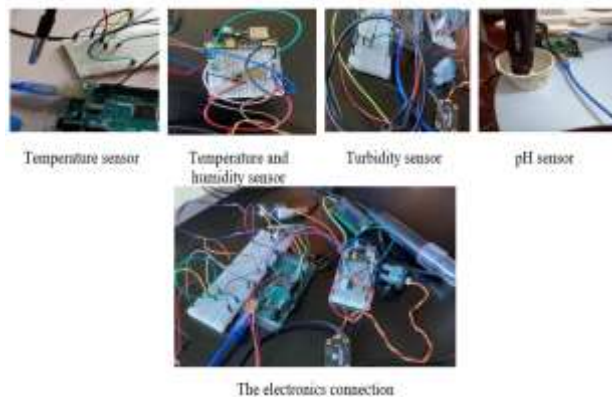


**Figure 5.** The electronics connection of the sensors on microcontroller



The temperature and pH values measured on the LCD are measured in different solutions and the results are compared. The water turbidity measurement value is also given in Figure 8. In this study, the temperature and humidity values of the environment/air were monitored. Temperature measurement values of the liquid were measured separately on serial monitor as shown in Figure 9.

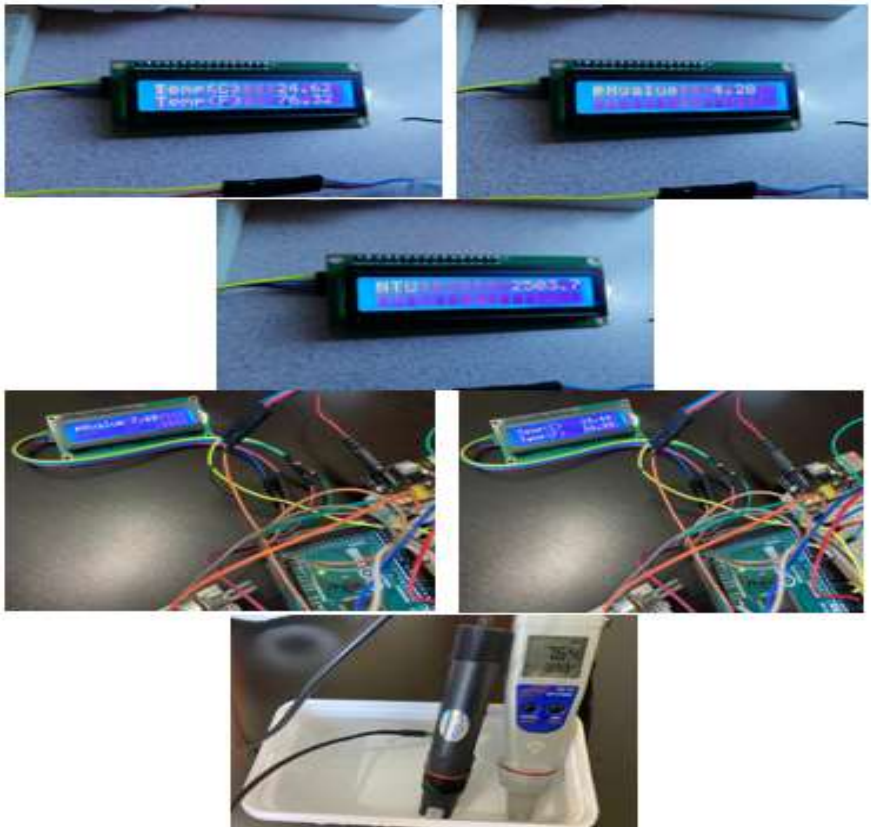


**Figure 8.** Temperature values, pH value and NTU value of the liquid and the comparison of measurements with a commercial device

```

Turbidity of Water NTU:2458.95
Temperature is: 25.75
Humidity: 37.70 %, Temp: 26.10 Celsius
Temperature:25.0^C pH:8.34
voltages1.86
Turbidity of Water NTU:2443.58
Temperature is: 25.62
Humidity: 37.80 %, Temp: 26.00 Celsius
Temperature:25.0^C pH:8.38
voltages1.86
Turbidity of Water NTU:2451.29
Temperature is: 25.62
Humidity: 38.00 %, Temp: 25.90 Celsius
Temperature:25.0^C pH:8.34
voltages1.86
Turbidity of Water NTU:2443.58
Temperature is: 25.62
Humidity: 37.90 %, Temp: 25.80 Celsius
Temperature:25.0^C pH:8.21

```

**Figure 9.** Measured values

Calibration process was carried out using the measurement results of the commercially purchased pH device. For this purpose, AD12 pH meter (ADWA kft.) pH meter was used (Figure 8). The size of the device is 175 x 39 x 23 (mm). The pH measurement range of the ADWA AD12 is in the range of -2.0 ~ 16.0 pH and temperature measurement range is -5 ~ 60 °C (23 ~ 140 °F). The sensitivity of the device is 0.1/0.01 pH; 0.1 °C / 0.1 °F and its accuracy is  $\pm 0.1/\pm 0.01$  pH; 0.5 °C /  $\pm 1$  °F.

Prior to the comparison, the calibration of the values measured by the designed device was achieved by use of a reference liquid with a known pH value (pH: 7.71) which was followed by the calibration of the commercial pH device. After both devices gave the same value, measurements were taken with two devices from two different buffer solutions and the difference has been determined as shown in Table 1 and Table 2.

<b>Table 1. pH measurements in buffer solutions</b>		
<b>Devices</b>	<b>Buffer solution (pH:5.00)</b>	<b>Buffer solution (pH:8.00)</b>
Commercial device	5.00	8.00
Designed device	5.00	7.99
Difference in pH	0.0	0.01
Percentage (%)	0.0 %	0.125 %

<b>Table 2. Temperature measurements and comparisons</b>	
<b>Devices</b>	<b>Temperature value (°C)</b>
Commercial device	23.80
Designed device	23.50
Difference	0.3
Percentage (%)	1.26 %

Several attempts have been made related to the utilization of low-cost Arduino-based systems for educational and scientific purposes. In one of these attempts, Qutieshat et al (2019) developed a cost-effective Arduino-based pH measurement device that enables visually impaired individuals to utilize and interpret universal pH paper by generating an audible tone when a RGB color sensor detects a change in the indicator's color. Their design involves the use of a color sensor and the auxiliary Arduino units. In another recent attempt, Ga et al. (2021) introduced an IoT friendly Arduino-based device to address major technical problems that students encounter during their scientific inquiry and proposed the utilization of physical computing and internet of things (IoT) technology as a counter measure. In another work Hong et al. (2021) introduced a prototype comprising of a microcontroller accompanied with multiple sensors to perform onsite measurements at

predefined intervals. Although the system was found to operate reliably, it was reported to be dependent on human intervention to tackle data inaccuracies. They also state that, the internet of things (IoT) friendly structure of their system allows its future use in this platform. The current work likewise introduces an IoT-friendly system, which does not only provide simultaneous monitoring of water quality parameters but also provides information about the quality of ambient air by use of a DHT sensor. This device is thus distinguished by simultaneous measurement of multiple media (water and ambient air) by use of a low-cost and IoT friendly Arduino-based system which can be used for educational, commercial, and academic purposes. The intrinsically IoT compatible structure of Arduino-based systems, such as the one introduced in this study, pave the way for their more extensive use such as remote monitoring and controlling of water and air quality, simultaneously. In this study, the portable pH meter measuring test device developed by using micro-controller card and (temperature, pH, turbidity) sensors and used in various applications was explained. Portable pH meters are used for fast and accurate measurement of pH value in laboratories, production environments and outdoor environments for environmental measurements. The system designed in this study consists of micro-controller, pH sensor, temperature sensor (DHT22 and DS18B20), turbidity detector and other electronic equipment.

## **CONCLUSION**

The aim of this study was to design a portable and ergonomically designed device that measures the pH value of various solutions and reflects them on the screen, and to test its reliability by testing it in different liquid environments (pH: 5.00, pH: 8.00). Compared with the test results with other trademarked devices, there was a difference of 0.0 % at pH: 5.00, 0.125 % difference at pH: 8.00 for pH and 1.26 % difference for temperature value. Considering that

this difference is due to software and hardware, it is thought to be an acceptable difference. It can be stated on the basis of the measurement results that, the designed device can successfully perform simultaneous measurement of multiple environmental parameters normally performed by separate devices by using a single microprocessor, thus reducing the cost. The proposed device is also distinguished from the similar works by measurement of the parameters of two different media (water and air) using a single microprocessor with an IoT friendly system structure and interface.

### **ACKNOWLEDGEMENTS**

This work is supported by Bartın University Research Fund project under the Project numbered: 2019-FEN-A-010/ and titled: “pH Meter Measurement Test Device Developed Using Micro-Controllers and Sensors” and it is performed within the scope of Bartın University’s Specialization Field: “Smart Logistics and Integrated Region Applications”.

## REFERENCES

- Abdellatif, M. M., Mohamed, W. 2020. "Telemedicine: An IoT Based Remote Healthcare System", *Int. J. Online Biomed. Eng. (iJOE)*, 16 (6), 72-81.
- Akar, F. (2018). "Arduino Gömülü Sistem Tasarımı (Embedded System Design) 1. Baskı", Beta Basım Yayım Dağıtım A.Ş., İstanbul, 1-324.
- Bahir, K. S. 2016. "Arduino Tabanlı Akıllı Ev Otomasyon Sistemi", *Yüzüncü Yıl Üniversitesi Fen Bilimleri Enstitüsü*, Van, 1-95.
- Çobanoğlu B. (2017). "Derinlemesine Arduino 1. Baskı", Abaküs Kitap Yayın Dağıtım Hizmetleri, İstanbul, 1-385.
- Daigavane, V. V., Gaikwad, M.A. 2017. "Water Quality Monitoring System Based on IOT", *Adv. Wirel. Mob. Com.*, 10 (5) 1107-1116.
- DF ROBOT, "Turbidity sensor SKUSEN0189" [https://wiki.dfrobot.com/Turbidity\\_sensor\\_SKU\\_\\_SEN0189](https://wiki.dfrobot.com/Turbidity_sensor_SKU__SEN0189) (Erişim tarihi: 20.07.2020)
- Dipova, N. 2017. "Açık Kaynaklı Geliştirme Platformlarının Geoteknik Laboratuvarı Çözümlerinde Kullanımı". *MAKÜ FEBED*, 8(2) 153-160.
- Dökmetaş, G. (2016). "Arduino ve Raspberry PI ile Nesnelerin İnterneti 1. Baskı", Dikeyksen Yayın Dağıtım, Yazılım ve Eğitim Hizmetleri San. Ve Tic. Ltd. Şti., İstanbul, 1-233.
- Ekmekci, H. D. 2017 "e-Health Kalkan ve Arduino Kullanılarak Çoklu Fizyolojik İşaretlerin Bilgisayar Ortamında Görüntülenmesi", Yüksek Lisans Tezi, *Afyon Kocatepe Üniversitesi Fen Bilimleri Enstitüsü*, Afyon, 1-75.
- Elverir, M. 2019 "Arduino ile Suyun Fiziksel parametrelerinden sıcaklık, pH ve Bulanıklık Verilerini Ölçen Taşınabilir bir Laboratuvar Ortamının Kurulması ve BOİ' nin Ölçülmesi", Yüksek Lisans Tezi, *Karabük Üniversitesi Fen Bilimleri Enstitüsü*, Karabük. 1-35.
- Ersin, Ç. 2015. "Arduino Mikrodenetleyici ve Güneş Enerjisi ile Çalışan Otomatik Bitki Sulama Sistemi", Yüksek Lisans Tezi,

*Süleyman Demirel Üniversitesi Fen Bilimleri Enstitüsü*, Isparta, 1-53.

- Fondriest Environmental Learning Center: Turbidity, Total Suspended Solids & Water Clarity <https://www.fondriest.com/environmental-measurements/parameters/water-quality/turbidity-total-suspended-solids-water-clarity/> Son Erişim Tarihi: 20.03.2021
- Ga, Seok-Hyun., Cha, Hyun-Jung., Kim, Chan-Jong., 2021. “Adapting Internet of Things to Arduino-Based Devices for Low-Cost Remote Sensing in School Science Learning Environments”, *iJOE*, Vol. 17, No. 02.
- Hong, W. J., Shamsuddin, N., Abas, E. et al., 2021. “Water Quality Monitoring with Arduino Based Sensors”, *Environments*, 8, 6.
- Järvinen T., Lorite, G. S., Rautio A.R., Juhász, K. L., Kukovecz, Á., Kónya, Z., Kordas, K., Toth, G. (2017). “Portable cyber-physical system for indoor and outdoor gas sensing”, *Sens. Actuators. B*, 252, 983–990.
- Karami, M., McMorrow, G. V., Wang L. 2018. “Continuous monitoring of indoor environmental quality using an Arduino-based data acquisition system”, *J. Build. Eng.*, 19: 412-419.
- Mashud, M. A. A., Masud, M. A., Islam, Md. S. (2011). “Design and Development of Microcontroller Based Digital pH Meter” *ULAB J. Sci. Eng.*, 2, 31-34.
- Netto, G. T., Arigony-Neto, J. 2019. “Open-source Automatic Weather Station and Electronic Ablation Station for measuring the impacts of climate change on glaciers”, *Hardware X*, e00053.
- Ntella, S. L. 2017. “Electronic System Design for Temperature and pH Measurements in Biomedical Applications”, Diploma Thesis, *Department of Electrical and Computer Engineering*, Aristotle University of Thessaloniki, Thessaloniki, 1-68.
- Özdemir, T. 2011. “Silikon detektörlerde benzetim, modelleme ve analiz süreçleri”, Doktora Tezi, *Süleyman Demirel Üniversitesi Fen Bilimleri Enstitüsü*, Isparta, 1-138.
- Özdemir Öge, T. 2018. “An Arduino-Based Automated Irrigation System Using Soil-Moisture Sensor and Air Temperature-Moisture Sensor”, 3rd International Conference on Material

Science and Technology in Cappadocia (IMSTEC'18), September 17-19, Nevşehir, Turkey.

- Rodriguez-Sanchez, M. C., Chakraborty, P., Malpica, N. (2020). "International collaborative projects on digital electronic systems using open source tools". *Comput. Appl. Eng. Educ.*, 1–11.
- Sevinç, H. (2015). "ESP8266 ve Arduino ile Nesnelerin İnterneti 1. Baskı", Dikeyksen Yayın Dağıtım, Yazılım ve Eğitim Hizmetleri San. Ve Tic Ltd. Şti, İstanbul, 1-115.
- Qian, H., Zhang, Q., Deng, Y. 2017. "Design of PH sensor signal acquisition and display system", *IOP Conf. Series: Earth and Environmental Science*, 69, 012082.
- Qutieshat, A., Aouididi, R., Arfaoui, R., 2019. "Design and Construction of a Low-Cost Arduino-Based pH Sensor for the Visually Impaired Using Universal pH Paper", *J. Chem. Educ.*, 96, 2333-2338.



## **CHAPTER 2**

### **INVESTIGATION OF APSIDAL MOTION OF DETACHED SYSTEMS RW LAC AND TV CET**

Dr. Muhammed Faruk YILDIRIM<sup>1,2</sup>

---

<sup>1</sup> Çanakkale Onsekiz Mart University, Astrophysics Research Center and Ulupınar Observatory, 17020, Çanakkale, Turkey. mf.yildirim@hotmail.com

<sup>2</sup> Çanakkale Onsekiz Mart University, Department of Electricity and Energy, Çan Vocational School, 17400, Çanakkale, Turkey. mf.yildirim@hotmail.com  
ORCID Code: (0000-0003-2382-7011)



## 1. INTRODUCTION

The classifications for the binary stars based on the Roche geometry and commonly used were made by Kopal (1955). This classification provides information on the evolution of stars. Accordingly, if both components do not fill the Roche lobes, they are called “detached binary stars (DB)”. In DB type systems the components are usually spherical and the maximum phases of the light curves appear almost flat (see Figure 1). DB systems are classified as Algol type in the classification made according to the light curve (LC) shape. The eclipses of the light curves of the Algol-type systems whose components are far from each other, whose spherical structures are intact and which have not evolved are quite sharp, and the depths of the eclipses are generally close to each other. Component temperatures of such young Algols are close to each other. In this study, the apsidal motion of two DB type systems (RW Lac and TV Cet) has been examined in detail.

The RW Lac (TIC 66355834, Gaia EDR3 1988664351633304320, TYC 3629-740-1) eclipsing binary system was discovered by Gaposchkin (1932) through photographic observations. Martinoff (1938) stated that its orbit is eccentric and it is stated that the orbital period is approximately 10 days. There is not much observation data in the literature regarding this system, which has a relatively long orbital period. In a comprehensive spectral and photometric study by Lacy et al. (2005), the astrophysical values of the RW Lac were reported. In the same study, they calculated the masses and radii of the components of the system ( $M_1=0.928\pm 0.006M_\odot$ ,  $M_2=0.870\pm 0.004M_\odot$  and  $R_1=1.186\pm 0.04R_\odot$ ,  $R_2=0.964\pm 0.004R_\odot$ ). In addition, Lacy et al. (2005) also prepared the O-C graph. In the period analysis study conducted by Wolf et al. (2006), the orbital period of the possible third component was found to be 7.2 (7) years.

The TV Cet (TIC 274039311, HD20173, Gaia EDR3 3268891057706416768, TYC 59-297-1) variable system was

discovered by Martynov (1951). The TV Cet is a rarely studied detached eclipsing system with a long orbital period of approximately 9 days. The first spectral studies of the system were made by Popper (1967, 1968), and it was classified as an F2 spectral star. In the light curve analysis performed by Bozkurt & Değirmenci (2010), the astrophysical values of the TV Cet were determined. In the same study they obtained the masses and radii of the components of the system ( $M_1=1.34\pm 0.05M_\odot$ ,  $M_2=1.23\pm 0.05M_\odot$  and  $R_1=1.47\pm 0.02R_\odot$ ,  $R_2=1.21\pm 0.02R_\odot$ ). In the period analysis conducted by Bozkurt & Değirmenci (2007), the apsidal motion period of the system was found to be  $25043\pm 11760$  years and was determined in a sinusoidal change.

## 2. DATA INFORMATION

It is very important to determine the minima times for DB systems of long orbital period. Therefore, TESS (Transiting Exoplanet Survey Telescope; Ricker et al. , 2015) data archived by MAST (Mikulski Archive for Space Telescopes, <https://archive.stsci.edu>) was used for the RW Lac and TV Cet systems. In both systems, light curve observations were made in the optical region with exposure times of 120 seconds. The observation of the RW Lac system was made in September 2019 for a period of one month (Sequence number: 16). Observations of the TV Cet system were made in October 2019 and 2020 for a period of one month (Sequence number: 4, 11). Data from TESS satellite is converted from BJD to HJD. The reason for the conversion is that most of the minima times in the literature are in HJD. The light curves from the database have been converted to a normalized flux and are given in Figure 1. Then the eclipse times were calculated and the eclipse times were calculated using the least squares method. The eclipse times and errors acquired from TESS data are given in Table 1. Four eclipse times and twelve minima times were calculated for RW Lac and TV Cet, respectively (see Table 1).

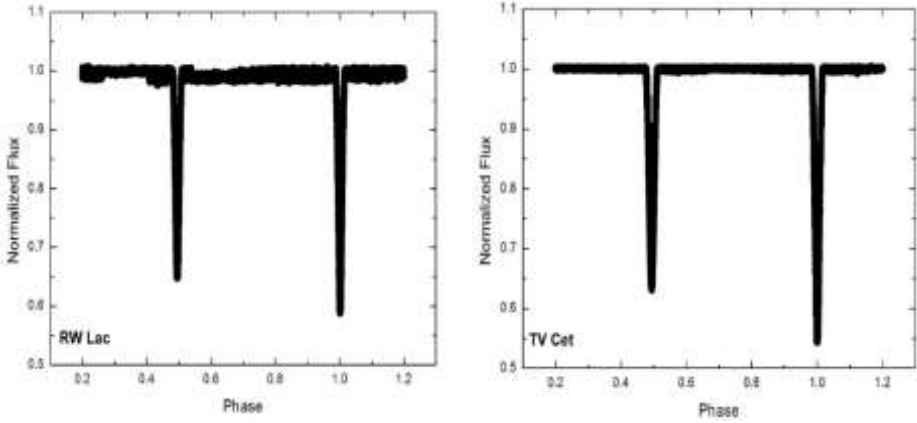


**Figure 1:** Light curves of RW Lac and TV Cet created with TESS data.

The eclipse times acquired from the TESS data, as well as the eclipse times published in the literature (mostly from the O-C Gateway (Paschke & Brat, 2006)) were collected and prepared for analysis. Basic astrophysical parameters for RW Lac and TV Cet systems were collected from the literature to be used in interpreting and discussing the analysis results and are listed in Table 2.

**Table 1.** Minima times of RW Lac and TV Cet detached systems calculated from TESS satellite data.

Systems	Minima Times (HJD+2400000)	Errors	Type (MinI/MinII)
RW Lac	58739.5581	0.0001	II
RW Lac	58744.8158	0.0001	I
RW Lac	58755.1850	0.0001	I
RW Lac	58760.2965	0.0001	II
TV Cet	58412.8481	0.0001	II
TV Cet	58417.4605	0.0001	I
TV Cet	58421.9515	0.0001	II
TV Cet	58426.5638	0.0001	I
TV Cet	58431.0547	0.0001	II
TV Cet	58435.6672	0.0007	I
TV Cet	59145.7255	0.0005	I
TV Cet	59150.2147	0.0001	II

TV Cet	59154.8272	0.0001	I
TV Cet	59159.3180	0.0001	II
TV Cet	59163.9304	0.0001	I
TV Cet	59168.4213	0.0001	II

**Table 2.** Basic parameters collected from literature for RW Lac and TV Cet detached systems.

System	Spectra l Type	Period (day)	$M_1/M_2$ ( $M_\odot$ )	$R_1/R_2$ ( $R_\odot$ )	$T_1/T_2$ (K)
RW Lac	G5+G7 <sup>1</sup>	10.3692046 (17) <sup>1</sup>	0.928 (6) <sup>1</sup>	1.186 (4) <sup>1</sup>	5760 (100) <sup>1</sup>
			0.870 (4) <sup>1</sup>	0.964 (4) <sup>1</sup>	5560 (150) <sup>1</sup>
TV Cet	F2-F3 <sup>2</sup>	9.1032891 (4) <sup>2</sup>	1.34 (5) <sup>2</sup>	1.47 (2) <sup>2</sup> 1.21 (1) <sup>2</sup>	6895 <sup>2</sup> 6570 (4) <sup>2</sup>
			1.23 (5) <sup>2</sup>		

**References:** 1: Lacy et al. (2005), 2: Bozkurt & Değirmenci (2010).

### 3. ORBITAL PERIOD ANALYSIS

The origins of period change in eclipsing binaries are principally mass exchange or mass loss, third-body effect, surface magnetic activity and apsidal motion. While mass transfer or loss and magnetic activity do really change the orbital period, while the third body and apsidal motion do not really change the orbital period. If there is a period change or which character it can be understood with O-C diagrams created by means of eclipse times. In this study, the O-C (Observed-Calculated) way, that is well recognized in the literature, was used for period analysis. For binary systems,  $T_o$  is the initial minimum time and  $P$  is the orbital period. The minima times may be calculated using by the formula bellow.

$$C=T_0+E.P \quad (1)$$

Here E is the epoch number. In both systems selected in this study, both the apsidal motion and a sinusoidal change were detected.

$$P_a = P_s \left(1 - \frac{\dot{w}}{360}\right)^{-1} \quad (2)$$

In Equation 2,  $P_s$ : represents the sidereal period of the system in days,  $P_a$ : the anomalistic period of the system in days,  $\dot{w}$ : the apsidal motion rate (degrees/cycle). Equation 3, that is well regenerated in the literature, is used to calculate the apsidal motion periods of the systems ( $U$  is in the unit of years).

$$U = \frac{360.P_a}{\dot{w}} \frac{1}{365.24} \quad (3)$$

The last orbital period analysis of the RW Lac detached binary was done by Wolf et al. (2006). Since the last study, a period analysis study was carried out with more up-to-date and more sensitive data of about 15 years. For RW Lac, an O-C graph was created by combining 4 new eclipse times acquired from TESS data with 55 eclipse times reported from in the literature. About half of these are the first minima times. We see that the change in the O-C graph acquired from the data distribution spanning about 100 years is apsidal motion and sinusoidal. Table 3 presents the results of the analysis. The O-C graphics of the RW Lac system obtained as a result of the analyzes are given in Figure 2 and Figure 3. The contribution of the third body to the apsidal motion was calculated as  $1.68 \times 10^{-7}$ %cycles.

The latest analysis of the TV Cet system was carried out by Bozkurt & Değirmenci (2007). Since the last study, a period analysis study was carried out with more up-to-date and more sensitive data of about 15 years. For TV Cet, an O-C diagram was created with 12 new eclipse times acquired from TESS data and 45 eclipse times reported from in

the literature. More than half of these are the first minima times. Analysis results are presented in Table 3. O-C diagrams of the TV Cet detached variable are given in Figure 4 and Figure 5. The contribution of the third body to the apsidal motion was calculated as  $3.96 \times 10^{-9}$  %/cycles.

**Table 3.** Parameters related to apsidal motion and third body effect obtained as a result of O-C analysis of RW Lac and TV Cet detached systems.

Parameters	RW Lac	TV Cet
$T_o$ (HJD+2400000)	52253.6442 (69)	52873.5268 (39)
$P_s$ (day)	10.369206 (5)	9.103291 (4)
$P_a$ (day)	10.369638 (5)	9.103696 (4)
$e$	0.014 (2)	0.010 (2)
$\dot{\omega}$ (deg/cycle)	0.015 (3)	0.016 (2)
$\omega$ (deg)	212 (11)	175 (5)
$U$ (year)	664 (60)	574 (35)
$a_{12} \sin i_3$ (AB)	2.9 (5)	0.29 (9)
$e_3$	0.42 (9)	0.37 (5)
$\omega_3$ (deg)	247 (12)	57 (15)
$A_3$ (day)	0.017 (4)	0.0017 (6)
$T_3$ (HJD+2400000)	60609 (240)	50840 (285)
$P_3$ (year)	22.5 (1.1)	33.5 (4.2)
$f(m_3)$ ( $M_\odot$ )	0.048 (3)	0.000023 (6)
$m_3$ ( $M_\odot$ ) (for, $i=90$ )	0.7	0.05

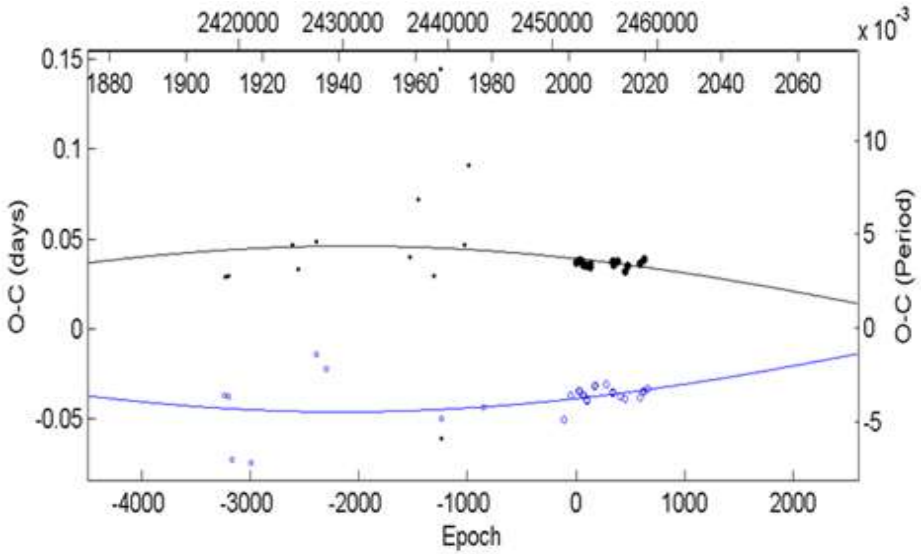


**Figure 2.** RW Lac's apsidal motion period change graph. Black and blue continuous lines indicate theoretical fit. Solid circles represent first eclipse times, and empty circles represent second eclipse times.

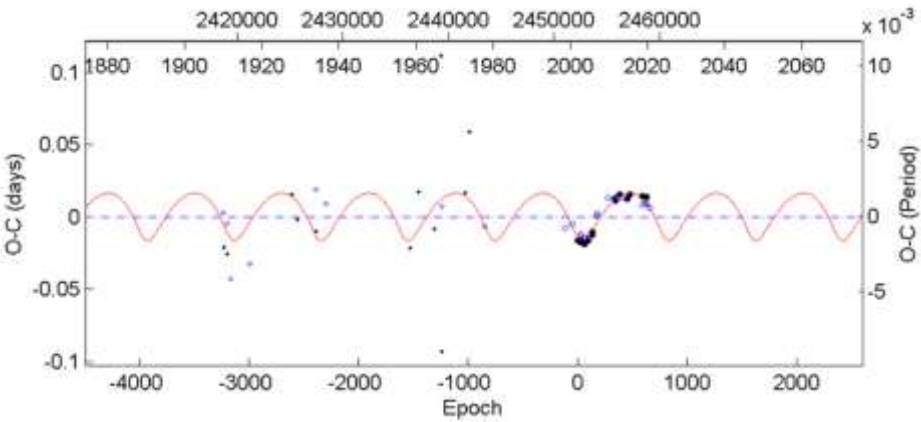


**Figure 3.** RW Lac's sinusoidal period change graph. The red continuous line shows the theoretical sinusoidal variation. The blue dotted line shows the theoretical parabola fit.

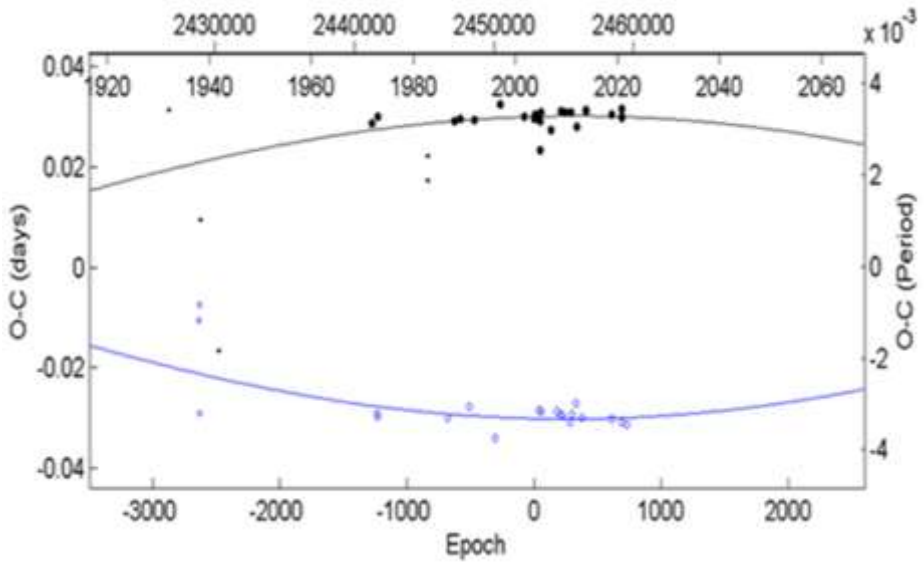


**Figure 4.** TV Cet's apsidal motion period change graph. Black and blue continuous lines indicate theoretical fit. Solid circles represent first eclipse times, and empty circles represent second eclipse times.

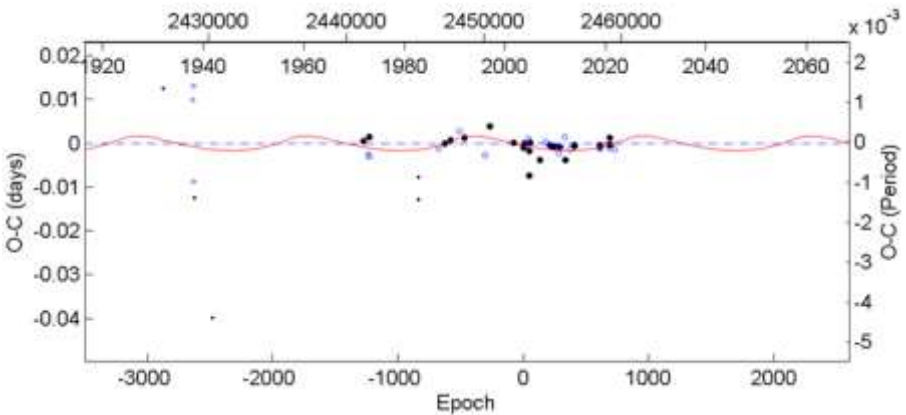


**Figure 5.** TV Cet's sinusoidal period change graph. The red continuous line shows the theoretical sinusoidal variation. The blue dotted line shows the theoretical parabola fit.

#### 4. RESULTS AND DISCUSSIONS

Minima times are very important for period analysis studies. It is especially important for systems with long orbital periods. Therefore, the TESS satellite data of the selected systems in this study has been an important source of motivation for us. 4 eclipse times (2 Min I and 2 Min II) for the RW Lac system and 12 eclipses (6 Min I and 6 Min II) for TV Cet were calculated (see Table 1). Results from this analysis are presented in Table 3 and the first 7 parameters in the Table 3 represent the apsidal motion period parameters, while the remaining parameters represent the possible third component parameters. Analysis of data distributed over approximately 100 years found the RW Lac system's apsidal motion period as 664 years and the eccentricity of the orbit as 0.014. The mass of the possible third body for RW Lac has been calculated to be about  $0.7 M_{\odot}$ . This value was greater than the value found by Wolf et al. (2006). Wolf et al (2006) determined the period of sinusoidal change to be 7.2 (7) years, and in this study it was determined as 22.5 years. This result shows the importance of newly added sensitive data calculated from TESS. For the TV Cet system, a period analysis was made using approximately 100 years of data. In the analyzes made, the axis rotation period of the system was found to be 574 years, and the orbital eccentricity was found to be approximately 0.010. The probable third body period for TV Cet has been calculated as approximately 33.5 years. The  $P_3$  value was much higher than the value found by Bozkurt & Değirmenci (2007), but the apsidal motion period was also smaller. The reason for these differences is the addition of new updated and more sensitive data. The probable third component mass calculated for the TV Cet ( $0.05M_{\odot}$ ) is below the star limit.

There are basically two contributions to the apsidal motion. The mutual gravitational effect of the component stars and the contribution from the rotation of the components are the primary source of contribution. The second source of contribution is the contribution predicted by the general theory of relativity. If there is a third object

connected to the system, it is predicted that it will affect the apsidal motion (Martynov 1948). The apsidal motion rate is measured by the change in the position of the periastron at the zero epoch of the binary star. In this case, the progression in the position of the periastron at the zero epoch of the system with a third component with a eccentricity orbital is expressed by the following equation.

$$\dot{w}_{obs} = \dot{w}_{rel} + \dot{w}_{classical} + \dot{w}_3 \quad (4)$$

In this equation,  $\dot{w}_{obs}$ : is the value obtained as a result of the analysis. The relativistic contribution ( $\dot{w}_{rel}$ ) in Equation 4 is given by Gimenez (1985) with the following expression.

$$\dot{w}_{rel} = 5.45 \times 10^{-4} \frac{1}{1-e^2} \left( \frac{M_1+M_2}{P} \right)^{2/3} \quad (5)$$

The value of  $\dot{w}_3$  is determined by the following equation given by Martynov (1948).

$$\dot{w}_3 = \frac{3}{8} \frac{M_3}{M_1+M_2+M_3} \left( \frac{P_s}{P_3} \right)^2 + \frac{225}{32} \left( \frac{M_3}{M_1+M_2+M_3} \right)^2 \left( \frac{P_s}{P_3} \right)^3 \quad (6)$$

The classical contribution ( $\dot{w}_{classical}$ ) was calculated by subtracting the observational value from the total value of these two contributions. Contributions to apsidal motion were calculated using Equations 4, 5, 6 for RW Lac and TV Cet and listed in Table 4. When we look at table 4, we find that the contribution of the classical contribution to the apsidal motion is more than 98%, while the contribution of the third body to the apsidal motion is negligible. In addition, the Relativistic contribution was observed to be negligibly small.

**Table 4.** Contributions and percentages for RW Lac and TV Cet detached eclipsing systems.

Parameters	RW Lac	TV Cet
$\dot{W}_{Obs}$	$1.5 \times 10^{-2}$	$1.6 \times 10^{-2}$
$\dot{W}_{classical}$	$1.48 \times 10^{-2}$	$1.58 \times 10^{-2}$
% contribution	98.87	98.53
$\dot{W}_{rel}$	$1.7 \times 10^{-4}$	$2.35 \times 10^{-4}$
% contribution	1.13	1.47
$\dot{W}_3$	$1.68 \times 10^{-7}$	$3.96 \times 10^{-9}$
% contribution	0.0011	0.000025

The eclipse times calculated for both systems made important contributions to the determination of both apsidal motion and sinusoidal change directions. Therefore, observations for eclipse times should be continued in order to better understand the nature and evolution of these two systems (RW Lac and TV Cet) in the future. In the future, both spectral studies and photometric studies will be very critical for RW Lac and TV Cet. Possible third components can be identified from spectral studies. From the photometric studies, both the light curve analysis can be updated and the new eclipse times to be calculated will be very important for apsidal motion and sinusoidal change.

## 5. ACKNOWLEDGEMENTS

In this paper, data archives of O-C Gateway (Paschke & Brat, 2006), Atlas O-C (Kreiner, 2004), Simbad (<http://simbad.u-strasbg.fr/simbad/>), TESS and MAST (<https://archive.stsci.edu>) were used. Therefore, we thank these working teams.

## REFERENCES

- Bozkurt Z. & Değirmenci Ö. L., 2007. Monthly Notices of The Royal Astronomical Society, 379, 370-378.
- Bozkurt Z. & Değirmenci Ö. L., 2010. New Astronomy, 15, 4, 356-361.
- Gaposchkin S., 1932. Veroeffentlichungen der Universitaetssternwarte zu Berlin-Babelsberg, 9, 1.
- Gimenez A., 1985. The Astrophysical Journal, 297:405-412.
- Kopal Z., 1955, Annales D' Astrophysique, 18, 379.
- Kreiner J. M., 2004. Acta Astronomica, 54, 207-210.
- Lacy C. H. S., et al., 2005. The Astronomical Journal, 130, 6, 2838-2846.
- Martinoff D.Y., 1938. Publ. Astron. Obs. Engelhardt, 20, 1.
- Martynov D. J., 1951. Publ. Engelhardt Obs., No. 26.
- Martynov D. Y., 1948. Izv. Engelhardt Obs. Kazan, No. 25.
- Paschke A. & Brat L. 2006. Open European Journal on Variable Stars, 23, 13-15.
- Popper D. M., 1967. Annual Review of Astronomy & Astrophysics, 5, 87.
- Popper D. M., 1968. Astrophysical Journal, 154, 191.
- Ricker, G. R., et al., 2015. Journal of Astronomical Telescopes, Instruments, and Systems, 1. 3.
- Wolf M. et al., 2006. Information Bulletin on Variable Stars, 5682, 1-4.

**CHAPTER 3**

**SURFACE AREA OF SUPERELLIPSOIDS AND ITS  
APPLICATION TO PHYSICS PROBLEMS**

Dr. Kadir Can ERBAŞ<sup>1</sup>

---

<sup>1</sup> Başkent University, Faculty of Engineering, Department of Biomedical Engineering, Ankara, Turkey, Email: kcerbas@gmail.com, ORCID: 0000-0002-6446-829X



## 1. INTRODUCTION

Superellipsoid is a general name given to a surface defined by Equation 1.1 (Maplesoft, 2021). The  $t$  and  $r$  values given in the equation are called the eastern and north exponents, and the parameters  $a$ ,  $b$ ,  $c$  are the half-axis lengths (Weisstein, 2021a). When these polar exponents are equal, they are also called superellipsoids (Gray, 1997). If  $t=r=n$  is assumed in Equation 1.1, Equation 1.2 is obtained as the equation of superellipsoids with equal pole exponents. Since this work is on equipolar superellipsoids, the term superellipsoid should be understood throughout the text as the surface in Equation 1.2. On this surface,  $n=2$  and infinity give the ellipsoid and prism, respectively. Values in between can be thought of as prisms with rounded corners. In the case of  $a=b=c$ , it is called a super spheroid and corresponds to the sphere and cube at  $n=2$  and infinity.

$$\left[ \left| \frac{x}{a} \right|^r + \left| \frac{y}{b} \right|^r \right]^{t/r} + \left| \frac{z}{c} \right|^t = 1 \quad (1.1)$$

$$\left| \frac{x}{a} \right|^n + \left| \frac{y}{b} \right|^n + \left| \frac{z}{c} \right|^n = 1 \quad (1.2)$$

Studies in recent years have shown that products with corners and sharp angles are less preferred than rounded designs. For this reason, the importance of convex superellipsoids ( $n>1$ ) in design and architecture has increased (Westerman et al., 2012, Silvia & Barona, 2009 and Bar & Neta, 2006). After the Danish scientist Piet Hein increased the popularity of superellipses in the 1960s, he generalized objects that were 3D versions of these shapes and called them superellipsoids or superspheres (Hein, 2021).

Superellipsoids are frequently used in architectural and industrial design (Westerman et al., 2012, Silvia & Barona, 2009 and Bar & Neta, 2006), preliminary design of fuselage (Flanagan & Hefner, 1967), contact mechanics calculations (Ambrosio, 2020), 3D computer

graphics design (Barr, 1981), railroad engineering (Magalhaes et al., 2020), granule packaging (Delaney & Cleary, 2010), medical imaging analysis (Bardinet et al., 1996), graphic modeling (Talu, 2011), object recognition (Andreopoulos & Tsotsos, 2012), computer vision and grasping for robotics (Varadarajan & Vincze, 2011 and Uckermann et al., 2012), contour surface modeling of boundary value problems (Erbaş, 2020 and Volpe & Khosla, 1990).

Many researchers have proposed the superellipse or superellipsoid approach for the solution of boundary value problems used in physics and engineering. In the study of decoding the eigenfrequencies of waveguides, Sun et al. showed that the first four eigenmodes of the elliptical guide and the magnetic field contours shown in the TM mode are shapes compatible with superquadrics (Sun et al., 2022). Volpe and Khosla FIRAS modeled the exponents ( $n$ ) of superellipsoidal contours as a function of position, by simulating the equipotential contour surfaces of the potential to superquadric surfaces [19]. Nagornov et al (Nagornov et al., 2021) and Huang et al (Huang et al., 2021) suggested rounding equipotential curves to superellipses in the applications of such boundary value problems used in physics. Especially in the last few years, shapes of the vibration modes of cracked nanoplate (Doan et al., 2022), streamlines and isotherms contours for nanofluid and water (Suresh, 2022), compression of Newtonian four-roll velocity distribution (Sedaghat et al., 2021) and spatial profiles of the electric potential (Jo et al., 2022) around cornered boundaries seems to be very similar to superellipses.

In order to generalize the three-dimensional version of the two-dimensional boundary value studies mentioned above, in this study, equipotential surfaces around a cube held at constant potential were modeled with superellipsoids and the capacitance of the unit cube was calculated. To do this, the surface area formulation of superellipsoids had to be known first. However, there is no surface area formulation for superellipsoids in the literature (Warnapala & Dinh, 2013), which

Khatib (Khatib, 1985) calls n-ellipsoid and appears to be widely used. Although the volume formula and other geometric properties are known (Jaklic et al., 2000), the lack of a surface area formula for such a widely used tool in physics is a major shortcoming. It is very difficult to model boundary value problems (Laplace, Helmholtz, wave equation, etc.) with superellipsoids because the surface area formulation is not known.

To address these important shortcomings in the literature, this study seek solutions to the following problems:

- Finding a numerical method that calculates the surface area of superellipsoids with complete accuracy,
- Obtaining a formula that calculates surface areas of convex superellipsoids very close to numerical results,
- Solving rectangular boundary value problems with this formula by modeling level curves with superellipsoids.

As a result, a method that provides a practical solution to rectangular boundary value problems has been developed with a formula that matches the surface area with numerical values very well. With the found formulation, the model, which was designed to provide an approximate solution to the boundary value problems, calculated the unit cube's capacitance, compared it with the values in the literature and tested its consistency.

## **2. SURFACE AREA OF SUPERELLIPSOIDS FOR N>1**

### **2.1 Numerical Calculations of the Surface Area**

In Cartesian coordinates, surface area of a smooth function  $z=f(x,y)$  onto a domain R is computed by the following:

$$S = \iint_R \sqrt{1 + \left(\frac{\partial z}{\partial x}\right)^2 + \left(\frac{\partial z}{\partial y}\right)^2} dA \tag{2.1}$$

The domain of the surface area integral may be taken as  $z=0$  cross-section in the first octant. However, this surface domain is very perpendicular at the boundary neighborhoods, its derivatives will approach infinity at the boundary, and the numerical integral in these regions will need a lot of iterations. As a matter of fact, when numerical integration is made directly on region R, it was seen that wrong results were obtained for some superellipsoids. This issue will be discussed further in the Results section. To avoid errors around the boundary regions where the surface is very perpendicular, it is preferred to calculate the surface area in some regions parallel to the domain as much as possible, taking advantage of the symmetry of superellipsoids. Figure 1 shows the division of the surface in the first octant into three distinct regions.

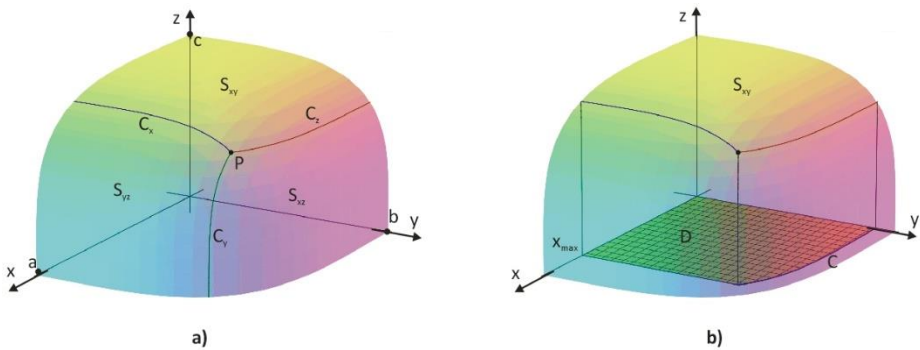


**Figure. 1** Images of a Superellipsoid in the First Octant. **A)** Point  $P$  Is The Intersection Of The Body Diagonal And The Surface, Level Curve  $C_z$  Is On  $Z=P_z$ , Level Curve  $C_y$  Is On  $Y=P_y$ , Level Curve  $C_x$  Is On  $X=P_x$ , And The Surface Segment  $S_{xy}$  Is Between  $C_x$  And  $C_z$ . **B)**  $D$  Is The Projection Of The  $S_{xy}$  Surface Segment Onto The  $Xy$  Plane And The  $C$  Is The Upper Bound Curve of  $D$ .

The 3D drawing of a superleipsoid in the first octant is shown in Figure 1.a and b. Point  $P$  is the point on the body diagonal and its coordinates can be found as follows.

$$\left(\frac{x}{a}\right)^n + \left(\frac{y}{b}\right)^n + \left(\frac{z}{c}\right)^n = 1 \rightarrow \left(\frac{x}{a}\right)^n = \left(\frac{y}{b}\right)^n = \left(\frac{z}{c}\right)^n = \frac{1}{3} \quad (2.2)$$

$$x = \frac{a}{3^{1/n}}, y = \frac{b}{3^{1/n}}, z = c \frac{c}{3^{1/n}}, \rightarrow P = (a, b, c) 3^{-\frac{1}{n}} \quad (2.3)$$

$$\begin{aligned} z = P_z = 3^{-\frac{1}{n}} c \rightarrow \left(\frac{x}{a}\right)^n + \left(\frac{y}{b}\right)^n + \frac{1}{3} &= 1 \\ \rightarrow \left(\frac{x}{a}\right)^n + \left(\frac{y}{b}\right)^n &= \frac{2}{3} \end{aligned} \quad (2.4)$$

$$\left(\frac{x}{a(2/3)^{1/n}}\right)^n + \left(\frac{y}{b(2/3)^{1/n}}\right)^n = 1 \quad (2.5)$$

This equation gives the level curve at  $z = P_z$ , and the part of it between  $x=0$  and  $x = x_{max} = 3^{(-1/n)}a$  is the C curve in Figure 1.b. Here, region D is expressed as the following:

$$\begin{aligned} D: 0 < y < b \left(\frac{2}{3} - \left(\frac{x}{a}\right)^n\right)^{1/n} \text{ and } 0 < x < x_{max} \\ &= 3^{-1/n} a \end{aligned} \quad (2.6)$$

Since the  $S_{xy}$  part is on region D, the surface area is found by the following equation.

$$\begin{aligned} S_{xy} \\ = \int_{x=0}^{x=a3^{-1/n}} dx \int_{y=0}^{y=b\left(\frac{2}{3} - \left(\frac{x}{a}\right)^n\right)^{\frac{1}{n}}} dy \sqrt{1 + c^2 \frac{\frac{x^{2n-2}}{a^{2n}} + \frac{y^{2n-2}}{b^{2n}}}{\left(1 - \left(\frac{x}{a}\right)^n - \left(\frac{y}{b}\right)^n\right)^{2-\frac{2}{n}}} } \end{aligned} \quad (2.7)$$

By swapping the axis lengths,  $S_{xy}$  to  $S_{xz}$  and  $S_{yz}$  can also be calculated. For example,  $S_{xz}$  is defined in a region D on  $xz$  and can be found by interchanging  $y$  and  $x$ .  $S_{xy}$  for the ellipsoid  $(x/b)^n + (y/c)^n + (z/a)^n = 1$  is equivalent to  $S_{yz}$  for Fig.1.a. Similarly,  $S_{xy}$  for the ellipsoid  $(x/c)^n + (y/a)^n + (z/b)^n = 1$  is equivalent to  $S_{xz}$  for Fig.1.a. Therefore, one can write Equations 2.8 and 2.9 for  $S_{yz}$  and  $S_{xz}$ .

$$\begin{aligned}
 & S_{yz} \\
 &= \int_{x=0}^{x=b3^{-1/n}} dx \int_{y=0}^{y=c\left(\frac{2}{3}-\left(\frac{x}{b}\right)^n\right)^{\frac{1}{n}}} dy \sqrt{1 + a^2 \frac{\frac{x^{2n-2}}{b^{2n}} + \frac{y^{2n-2}}{c^{2n}}}{\left(1 - \left(\frac{x}{b}\right)^n - \left(\frac{y}{c}\right)^n\right)^{2-\frac{2}{n}}} } \quad (2.8)
 \end{aligned}$$

$$\begin{aligned}
 & S_{xz} \\
 &= \int_{x=0}^{x=c3^{-1/n}} dx \int_{y=0}^{y=a\left(\frac{2}{3}-\left(\frac{x}{c}\right)^n\right)^{\frac{1}{n}}} dy \sqrt{1 + b^2 \frac{\frac{x^{2n-2}}{c^{2n}} + \frac{y^{2n-2}}{a^{2n}}}{\left(1 - \left(\frac{x}{c}\right)^n - \left(\frac{y}{a}\right)^n\right)^{2-\frac{2}{n}}} } \quad (2.9)
 \end{aligned}$$

The total surface area in the first octant is the sum of  $S_{xy}$ ,  $S_{xz}$  and  $S_{yz}$  so the whole surface areas of the superellipsoid with semi axis  $a$ ,  $b$ , and  $c$  is the eight times the sum as in Equation 2.10.

$$S = 8(S_{xy} + S_{xz} + S_{yz}) \quad (2.10)$$

The surface area of a general superellipsoid shown in Equation 2.1-2.10 was computed with the MATLAB whose scripts are given in Appendix A.

## 2.2 Approximate Formula for the Surface Area of Superellipsoids

To obtain a formula that gives a good approximation of the surface areas of superellipsoids, the surface area formulas of two special super ellipsoids, the octahedron ( $n=1$ ) and the rectangular prism ( $n=\infty$ ), were taken as basis. Surface area formulas for these special superellipsoids are given below.

$$\begin{aligned}
 S_1 &= 4\sqrt{a^2b^2 + a^2c^2 + b^2c^2} \\
 &= 2A_1(1,1)(a^2b^2 + a^2c^2 + b^2c^2)^{1/2} \quad (2.11)
 \end{aligned}$$

$$\begin{aligned}
S_\infty &= 8(ab + ac + bc) \\
&= 2A_\infty(1,1)(a^1b^1 + a^1c^1 + b^1c^1)^{1/1}
\end{aligned} \tag{2.12}$$

$A_I(I,I)$  and  $A_\infty(I,I)$  are areas of regular super-ellipses with unit radius ( $a=b=I$ ) of degree 1 and infinity because when  $c=0$ , a double super-ellipse with  $a$  and  $b$  half-axis is formed. Since these degrees correspond to rhombus and square, their areas are  $A_I(I,I)=2$  and  $A_\infty(I,I)=4$ , respectively. Equation 2.13 is the approximate ellipsoid surface area formula proposed by Knud Thomsen, where it has a value of  $p=1.6$  (Michon, 2020). As a generalization of Equation 2.11-13, the approximate surface area formula of any degree  $n$  superellipsoid can be assigned as in Equation 2.14. Here,  $s(n)$  is a degree-dependent exponent and  $A_n(I,I)$  is the area of the superellipse in which both the half-axis lengths are equal to one at this degree. The exact formulation of the area of a super ellipse can be seen in Eq.14a (Weisstein, 2021b) but since this is a complex formula, Equation 2.15b can be suggested instead. The exponent  $s(n)$  as a function of  $n$  (Eq.2.14b) was obtained by surface fit and curve fit methods applying to the numerical surface areas.

$$\begin{aligned}
S_2 &= 2\pi(a^p b^p + a^p c^p + b^p c^p)^{1/p} \\
&= 2A_2(1,1)(a^{1.6}b^{1.6} + a^{1.6}c^{1.6} \\
&\quad + b^{1.6}c^{1.6})^{1/1.6}
\end{aligned} \tag{2.13}$$

$$S_n = 2A_n(1,1)(a^{s(n)}b^{s(n)} + a^{s(n)}c^{s(n)} + b^{s(n)}c^{s(n)})^{1/s(n)} \tag{2.14}$$

$$A_n(1,1) = 4^{(1-1/n)}\sqrt{\pi} \frac{\Gamma(1 + 1/n)}{\Gamma(1/2 + 1/n)} \tag{2.14a}$$

$$s(n) = 1 + \frac{n - 0.6599}{n^2 - 1.048 * n + 0.3882} \tag{2.14b}$$

A second alternative (Equation 2.15) for Eq.2.14 is proposed by including one more parameter that can explain the surface area. In Eq.2.15, values of  $\alpha_n$  at  $n=1$  and infinity are  $\alpha_1=0$ ,  $\alpha_\infty=0$  and  $s_1=1$ ,  $s_\infty=1/2$ . Ratios of the axis lengths are assigned as  $p=b/a$  and  $q=c/a$ . Since  $a \geq b \geq c$ , the ratios must satisfy  $1 \geq p \geq q$  in Equation 2.15.

$$S_n = 2a^2 \cdot A_n(1,1) \left( p^{2s(n)} + q^{2s(n)} + p^{2s(n)}q^{2s(n)} + \alpha(n) \cdot p^{s(n)}q^{s(n)}(1 + p + q) \right)^{1/(2s(n)} \quad (2.15)$$

$$s(n) = \frac{0.5 \cdot n^2 - 0.06251 \cdot n - 0.3028}{n^2 - 1.083 \cdot n + 0.2178} \quad (2.15a)$$

$$A_n(1,1) = \frac{4 \cdot n^2 + 4.59 \cdot n - 2.368}{n^2 + 1.148 \cdot n + 0.9642} \quad (2.15b)$$

$$\alpha(n) = \frac{-0.001362 \cdot n^2 - 0.03787 \cdot n + 0.03992}{n^2 - 2.36 \cdot n + 1.822} \quad (2.15c)$$

It was seen that Equation 2.15 yields more approximate results than Eq.2.14 when they were fitted for the surface area of the ellipsoid ( $n=2$ ) so Equation 2.15 was preferred to represent the surface area of a superellipsoid. Another version of Eq.2.15 can be written as Eq.2.16. All the formulas suggested in Equations 2.11-16 were found by fitting the numerical results using MATLAB surface fit and curve fit tools, and their details will be discussed in the Results section.

$$S_n = 2 \cdot A_n(1,1) \left( (ab)^{2s(n)} + (ac)^{2s(n)} + (bc)^{2s(n)} + \alpha(n) \cdot a^{2s(n)}b^{s(n)}c^{s(n)}(1 + b/a + c/a) \right)^{1/(2s(n)} \quad (2.16)$$

### 3. CALCULATION OF THE CAPACITANCE OF A UNIT CUBE

As an example of the use of superellipsoids in physics problems, equipotential surfaces around the unit cube held at constant potential can be modeled with superellipsoids whose degree varies depending on location. The cube itself represents the degree of infinity ( $n \rightarrow \infty$ ), and the equipotential surface at infinity represents the sphere ( $n=2$ ). Superellipsoid families whose degree decreases from infinity to two as one moves away from the position of the cube to infinity can be approximated by equipotential curves around the cube held at constant potential (Fig.2). Super ellipsoid families with equal half-axis lengths ( $a=b=c=u$ ) are given in equation 3.1 (Erbaş, 2020 and Durufle et al., 2014).

$$x^{n(u)} + y^{n(u)} + z^{n(u)} = u^{n(u)} \tag{3.1}$$

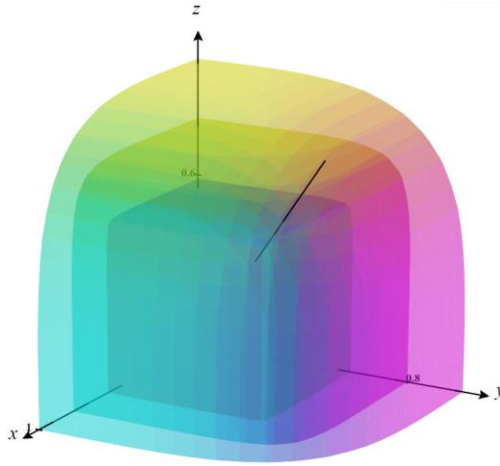


**Figure. 2** Superellipsoids With Varying Degrees ( $n$ )

The parameter  $u$  in Equation 3.1 represents the radius of the superellipsoid, and  $n(u)$  represents the degree as a function of the radius. In order to estimate the  $n(u)$  function here, the body diagonals of the superellipsoids are used. Since the body diagonal will pass through  $x=y=z$  points, the distance ( $L$ ) of the body diagonal to the origin is calculated as shown in equations 3.2 and 3.3.

$$x^{n(u)} + x^{n(u)} + x^{n(u)} = u^{n(u)} \rightarrow 3x^{n(u)} = u^{n(u)} \rightarrow x = u 3^{-1/n} \quad (3.2)$$

$$L = \sqrt{3} x = u 3^{1/2-1/n} \quad (3.3)$$

Assuming that the electric potential around the cube is a univariate function that only depends on  $u$ , the electric field magnitude, which is the potential gradient, must also depend only on  $u$ . Taking the two linear gradient lines as the x-axis and body diagonal, the infinitesimal lengths  $ds$  on these lines must be equal. Here, the  $ds$ -thick layer can be compared to a cell membrane of constant thickness [32]. Therefore, the difference between the semi diagonal length ( $L$ ) and radius ( $u$ ) must be constant. This constant can be calculated from the *semidiagonal length – radius* of the unit cube as in Eq. 3.4 (see Fig.3 for details). One can read refs. 18 and 32 for the two dimensional version (Erbaş, 2020 and Erbaş 2019).

$$dL = du \rightarrow L - u = const. \rightarrow u 3^{1/2-1/n} - u = 0.5(\sqrt{3} - 1) \quad (3.4)$$

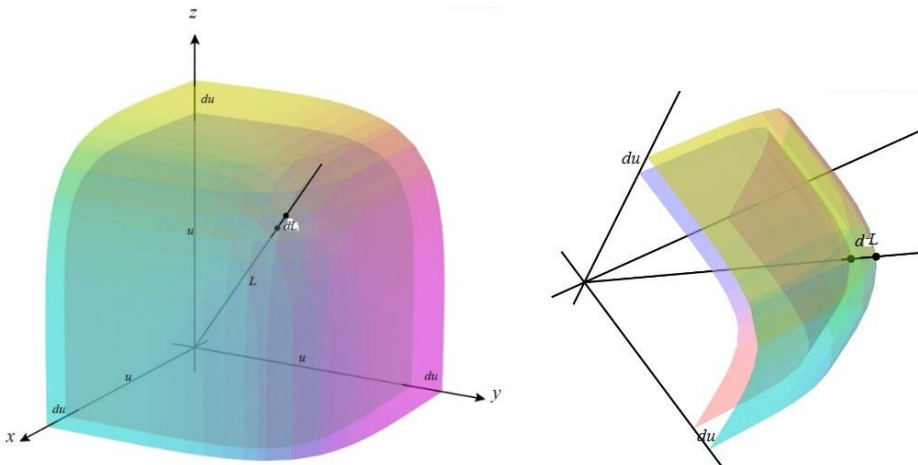


**Figure. 3** Two Neighboring Equipotential Surfaces At  $U$  And  $U+Du$ .  $L$  Is The Semi Body Diagonal Length And  $U$  Is The Radius From Different Perspectives.

From Eq. 3.4, degree of the super ellipsoids as a function of radius is given by

$$n(u) = \frac{\ln 3}{\ln \left( \frac{\sqrt{3} u}{u + 0.5(\sqrt{3} - 1)} \right)}. \quad (3.5)$$

To verify the assumptions described above, the capacitance of the unit cube was calculated using Equation 3.5 and compared with the values in the literature. Gauss's law was used as follows to calculate the capacitance with the superellipsoid approach. When any super ellipsoidal equipotential surface is determined as a Gaussian surface, Eq. 3.6 is written. Since the Gaussian surface is an equipotential, it is always perpendicular to the field lines and is constant in magnitude, so the integral in Equation 3.6 can be written as *electric field x surface area*. Parameters  $S$ ,  $q$ ,  $E$  and  $\epsilon_0$  denote the surface area of the superellipsoid, charge on the cube, electric field and permittivity of vacuum.

$$\oiint \vec{E} \cdot d\vec{A} = E \cdot S = \frac{q}{\epsilon_0} \rightarrow -\frac{dV}{du} \cdot S(u) = \frac{q}{\epsilon_0} \quad (3.6)$$

From Eq. 3.6, potential difference between the cube and the infinity is given by

$$\Delta V = -\frac{q}{\epsilon_0} \int_{u=0.5}^{\infty} \frac{du}{S(u)}. \quad (3.7)$$

The definition of capacitance can be written as Eq. 3.8, surface area as a function of radius  $S(u)$  and surface area of the unit spheroid are given in Equations 3.9 and 3.10.

$$C = \frac{q}{\Delta V} = \frac{\epsilon_0}{\int_{\infty}^{0.5} \frac{du}{S(u)}} \quad (3.8)$$

$$S(u) = u^2 S_{11}(n) \quad (3.9)$$

$$S_{11}(n) = 2A_n(3 + 3\alpha_n)^{\frac{1}{2S(n)}} \quad (3.10)$$

Combining Equations 2.15, 3.9, 3.10 into Eq.3.8 gives the value of the capacitance as 78.2802 pF, which is very close to literal values. The details of the computation can be seen in Appendix B as a MATLAB script.

## 4. RESULTS AND DISCUSSIONS

### 4.1. Surface Area Formula for Superellipsoids

The surface area of a superellipsoid can be computed by the direct integration in Eq.2.1 over the region R, which is a xy plane cross-section of the superellipsoid. However, this has some limitations. Partial derivatives over the near-boundary of the domain R diverge so the computation of the surface area gets harder. As a proof of this, the complex number  $0.8928 + 0.0367i$  is obtained by directly integrating the surface area of an ellipsoid ( $n=2$ ) with half-axis lengths  $a=0.9$ ,  $b=0.1$ ,  $c=0.1$ . However, when the surface is divided into three segments and integrated numerically (as Equation 2.10), the area is computed as 0.8933. For a correct comparison, with the surface area formula given for the ellipsoid, different extreme values for  $n=2$  were calculated numerically and analytically. The surface area formula for the ellipsoid ( $n=2$ ) is shown in equations 4.1 and 4.2

$$S = 2\pi \left( c^2 + b\sqrt{a^2 - c^2} E(\varphi, K) + b c^2 \frac{F(\varphi, K)}{\sqrt{a^2 - c^2}} \right) \quad (4.1)$$

$$\varphi = \arcsin \left( \sqrt{1 - \frac{c^2}{a^2}} \right), \quad K = \frac{a^2(b^2 - c^2)}{b^2(a^2 - c^2)} \quad (4.2)$$

where  $F$  and  $E$  are the elliptic integrals of the first and second kinds (Jaklic et al., 2020 and Erbaş, 2019). Eq. 4.1 gives the surface area of  $a=0.9$ ,  $b=0.1$ ,  $c=0.1$  as  $0.8933$ , which is the same as Eq.2.10. These results showed that finding the surface area by direct integration will give erroneous results in some extreme ellipsoids, but instead, taking numerical integration by segmenting as in equation 2.10 will give more precise results. For this reason, the method in Equation 2.10 was used for all superellipsoid surface area calculations throughout the study. This method is shown in Appendix A.

For a more precise surface area, the numerical method given in equation 2.10 was calculated for different  $n$  values and different semi-axis lengths. Half axis lengths were selected for  $a=1>b>c$  from the set  $(p,q)$  in Eq.4.3. The  $n$  values are chosen as in Equation 4.4.

$$(p, q) = \{0.1, 0.2, 0.3, 0.4, 0.5, 0.6, 0.7, 0.8, 0.9, 1.0\} \times \{0.1, 0.2, 0.3, 0.4, 0.5, 0.6, 0.7, 0.8, 0.9, 1.0\} \quad (4.3)$$

$$n = \left\{ \begin{array}{l} 1.1, 1.2, 1.3, 1.4, 1.5, 1.7, 1.8, 2.0, 2.2, \\ 2.4, 2.7, 3.0, 3.4, 4.6, 5.5, 6.0, 7.0, 8.5, 9.0, 11.5, 12, 18, 36 \end{array} \right\} \quad (4.4)$$

For the  $p$  and  $q$  values corresponding to each  $n$  value, the surface area was calculated with the numerical method in Equation 2.10, and the surface areas for each  $n$  value were fitted to both Equation 2.14 and 15 with surface fit. For example, the surface fit for the surface areas of the  $p$  and  $q$  values in Eq.4.3 for the  $n=2$  value is shown in Figure 4.

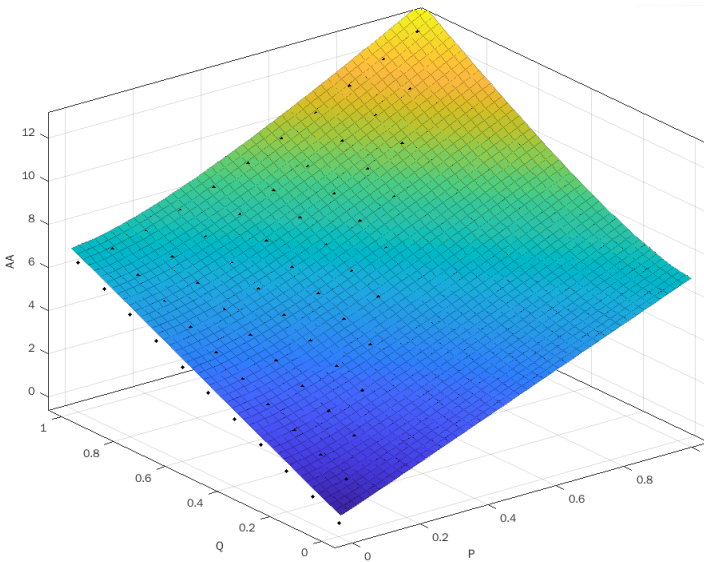


**Figure 4:** Surface fit Output of  $N=2$  for the  $P$  and  $Q$  Values in Eq. 4.3.

$A_n$ ,  $s_n$  and  $\alpha_n$  values in Equations 2.14-16 were calculated for each  $n$  in equation 4.4 and the obtained values were fitted with  $n$  values using MATLAB curve fitting tool. The results of these curve fittings are shown in Table 1.

**Table 1:** Goodness of Fit for Eq.2.15

	$s(n)$ Eq.2.14b	$A_n$ (Eq.15b)	$s(n)$ (Eq.15b)	$\alpha_n$ (Eq.2.15c)
SSE:	7.198e-005	3.302e-006	8.561e-006	8.403e-006
R-square:	1	1	1	0.9978
RMSE:	0.001897	0.0004407	0.0007096	0.0007031

Comparisons of the approximate formula given in Equations 2.14 and 2.15 for some extreme values with numerical method are given in Table 2 and 3. The mean absolute percentage errors are found as 0.246% and 0.177% respectively

**Table 2:** Percentage Errors Of Eq.2.14 Relative To The Numerical Results And The Mean Absolute Percentage Error (MAPE) For Each  $N$  And  $(P,Q)$  Values.

$n \backslash (p,q)$	(0.1, 0.1)	(0.1, 0.9)	(0.4, 0.6)	(1.0, 1.0)	MAPE
1.1	-0.14485	0.004538	-0.10976	-0.14001	0.09979
1.5	-0.61558	0.205722	-0.00077	0.05111	0.218295
2.0	-1.05502	0.23939	-0.0907	0.014333	0.349862
2.5	-1.20905	0.163424	-0.17551	-0.0568	0.401196
4.0	-1.12244	-0.00826	-0.21921	-0.1065	0.3641
6.0	-0.87229	-0.06871	-0.16522	-0.07194	0.294541
10.0	-0.56969	-0.07154	-0.08869	-0.02212	0.188011
36.0	-0.16482	-0.02587	-0.01128	0.011066	0.053259
MAPE	0.719218	0.098432	0.107642	0.059234	0.246132

**Table 3:** Percentage Errors Of Eq.2.15 Relative To The Numerical Results And The Mean Absolute Percentage Error (MAPE) For Each  $N$  And  $(P,Q)$  Values.

$n \backslash (p,q)$	(0.1, 0.1)	(0.1, 0.9)	(0.4, 0.6)	(1.0, 1.0)	MAPE
1.1	-0.093	-0.009	-0.093	-0.114	0.077
1.5	-0.463	-0.045	-0.007	0.003	0.130
2.0	-0.880	-0.052	-0.067	-0.102	0.275
2.5	-0.903	0.002	0.047	0.023	0.244
4.0	-0.761	0.020	0.119	0.114	0.254
6.0	-0.612	-0.023	0.074	0.070	0.195
10.0	-0.446	-0.066	0.007	-0.001	0.130
36.0	-0.199	-0.086	-0.077	-0.097	0.115
MAPE	0.545	0.038	0.061	0.066	0.177

According to the percentage errors in Tables 2 and 3, it is seen that the most inaccurate values belong to the pen-like prolate super ellipsoids whose  $b$  and  $c$  lengths are much smaller than  $a$ . The mean absolute percentage errors (MAPE) of this type are 0.719% and 0.545% respectively. The best results of Eq.2.15 were obtained using the oblate superellipsoids and the mean absolute percentage errors are 0.038% and that of Eq.2.14 is 0.059% for super spheroids. As for the exponents of superellipsoids, it has been observed that the most accurate estimates

are  $n=1$  and *infinity*, and the error increases as it becomes spherical. Tables 2 and 3 show that there is an average absolute percentage error of 0.275% for  $n=2$ . When a general evaluation is made, it can be said that the mean absolute percentage error is around 0.246%, the errors are less than 1.209% for Eq.2.14 and 0.177%, the errors are less than 0.903% for Eq.2.15.

#### 4.2. Capacitance of a Unit Cube

As an example of a physical application of superellipsoids, the capacitance of the unit cube was calculated as  $0.704 \times 4\pi\epsilon_0 = 78.28 \text{ pF}$  using the method described in Chapter 3. There are many suggestions for the capacitance values of the unit cube calculated in the literature. When the studies on this subject are examined, it is seen that the capacitance is calculated as a minimum of 72.9342 pF and a maximum of 80.6 pF (Maas, 1994). While the average of the values mentioned in the literature corresponds to approximately 73.4862 pF, the arithmetic average of the maximum and minimum values was calculated as 76.7671 pF. The value calculated in this study, 78.28 pF, was 6.5% greater than the literature average and 1.97% greater than the maximum minimum midpoint. First of all, the calculated value was between the limit values in the literature. For details of capacitance results in the literature, the reader may see ref. (Canas et al., 2009, Wintle 2004, Hwang & Mascagni, 2004, Bai & Lonngren 2002 and Ruehli & Brennan, 1973).

#### 5. CONCLUSION

This study yielded three findings regarding convex superellipsoids. These are, in order: a numerical method for the surface area, which has been tested for accuracy, a surface area formula that gives similar results with the numerical method with less than 1% error, and a modeling that describes the level surfaces formed around the cubic boundary with convex super-ellipsoids. In order to test the accuracy of

this modeling, the capacitance of the unit cube was calculated with Gauss's law and the surface area formula found, and results very close to the values in the literature were obtained. If this work is advanced, the solution of rectangular boundary value problems can be simplified using superellipsoids and a simple approximation method can be developed for cornered boundary value problems.

## APPENDIX A: MATLAB SCRIPT FOR THE SURFACE AREA CALCULATIONS

```
clear; clc; n=2; a=1; b=0.75; c=0.28; % degree and dimensions of the
superellipsoid
% Surface area computation over the region R (direct numeric
integration Eq.2.1)
r=a; p=b; q=c; xmax=1; ymax = @(x) p*(1-(x/r).^n).^(1/n);
I = @(x,y) sqrt(1+(q^2*r^(-2*n).*x.^(2*n-2) + q^2*p^(-2*n).*y.^(2*n-
2))./(1-(x/r).^n-(y/p).^n).^(2-2/n));
S2_1 = 8*integral2(I,0,xmax,0,ymax)
% Surface area computation over the region D (equation 2.10)
r=a; p=b; q=c; xmax=r*3.^(-1/n); ymax = @(x) p*(2/3-(x/r).^n).^(1/n);
Ixy = @(x,y) sqrt(1+(q^2*r^(-2*n).*x.^(2*n-2) + q^2*p^(-
2*n).*y.^(2*n-2))./(1-(x/r).^n-(y/p).^n).^(2-2/n));
Sxy = 8*integral2(Ixy,0,xmax,0,ymax);
r=b; p=c; q=a; xmax=r*3.^(-1/n); ymax = @(x) p*(2/3-(x/r).^n).^(1/n);
Iyz = @(x,y) sqrt(1+(q^2*r^(-2*n).*x.^(2*n-2) + q^2*p^(-
2*n).*y.^(2*n-2))./(1-(x/r).^n-(y/p).^n).^(2-2/n));
Syz = 8*integral2(Iyz,0,xmax,0,ymax);
r=c; p=a; q=b; xmax=r*3.^(-1/n); ymax = @(x) p*(2/3-(x/r).^n).^(1/n);
Ixz = @(x,y) sqrt(1+(q^2*r^(-2*n).*x.^(2*n-2) + q^2*p^(-
2*n).*y.^(2*n-2))./(1-(x/r).^n-(y/p).^n).^(2-2/n));
Sxz = 8*integral2(Ixz,0,xmax,0,ymax);
S2_1=Sxy+Syz+Sxz
```

```

% FOR ONLY n=2. Surface area computation from the ellipsoid (n=2)
formula (equation 4.1)
%http://www.numericana.com/answer/ellipsoid.htm
fi=asin(sqrt(1-c.^2./a.^2)); K=(a^2*(b^2-c^2)/(b^2*(a^2-c^2)));
S4_1=2*pi*(c^2 + b*sqrt(a^2-c^2)*ellipticE(fi,K) +
b*c^2*ellipticF(fi,K)/sqrt(a^2-c^2))

```

## APPENDIX B: MATLAB SCRIPT FOR THE COMPUTATION OF CAPACITANCE

```

% Capacitance of Unit Cube
a=0.5; % radius of the unit cube
u=[0.500:0.1:500]'; n=2*log(3)./log(3./(1+a*(sqrt(3)-1)./u).^2);
S1n=2*(4*n.^2 + 4.59*n - 2.368)./(n.^2 + 1.148*n + 0.9642).*(3+3*(-
0.001362*n.^2 -0.03787*n + 0.03992)./(n.^2 -2.36*n + 1.822)).^(n.^2
-1.083*n + 0.2178)./(n.^2 -2*0.06251*n -2*0.3028));
I=1./(u.^2.*S1n); II=cumtrapz(u,I);
C_frd=8.85/II(end)
C4pi=1/(4*pi*II(end))

```

## REFERENCES

- Ambrosio, J. (2020). A general formulation for the contact between superellipsoid surfaces and nodal points. *Multibody System Dynamics*, 50(4), 415-434.
- Andreopoulos A. and Tsotsos J. K. (2012). "A Computational Learning Theory of Active Object Recognition Under Uncertainty," *International Journal of Computer Vision*, vol. 101, no. 1, pp. 95–142.
- Bardinet E., Cohen L. D., and Ayache N., (1996). "Tracking and motion analysis of the left ventricle with deformable superquadrics." *Medical image analysis*, vol. 1, no. 2, pp. 129–149.
- Bai, E. W., & Lonngren, K. E. (2002). On the capacitance of a cube. *Computers & Electrical Engineering*, 28(4), 317-321.
- Barr, A. H. (1981). Superquadrics and angle-preserving transformations. *IEEE Computer graphics and Applications*, 1(1), 11-23.
- Bar, M., & Neta, M. (2006). Humans prefer curved visual objects. *Psychological science*, 17(8), 645-648.
- Canas-Penuelas, C. S., Catalan-Izquierdo, S., Bueno-Barrachina, J. M., & Cavalle-Sese, F. (2009). Unit cube capacitance calculation by means of finite element analysis. In *International Conference on Renewable Energies and Power Quality, Valencia (Spain)*, 15th to 17th April.
- Delaney, G. W., & Cleary, P. W. (2010). The packing properties of superellipsoids. *EPL (Europhysics Letters)*, 89(3), 34002.
- Doan, D. H., Zenkour, A. M., & Van Thom, D. (2022). Finite element modeling of free vibration of cracked nanoplates with flexoelectric effects. *The European Physical Journal Plus*, 137(4), 1-21.

- Durufle, M., Peron, V., & Poignard, C. (2014). Thin layer models for electromagnetism. *Communications in Computational Physics*, 16(1), 213-238.
- Erbaş K.C. (2019). Reducing the Laplace Equation to a 1D Problem in a Square Shaped Boundary, ICCMAS2019 International Conference on Computational Methods in Applied Sciences, İstanbul, Turkey, July 2019, p. 284.
- Erbaş K.C. (2020). Calculation of the characteristic impedance of a square coaxial line by fitting the equipotential curves to the super circles, 1st international Ankara multidisciplinary studies congress, Ankara, Turkey, August 2020, pp. 115-125
- Flanagan, D. L., & Hefner, O. V. (1967). Surface molding- New tool for the engineer (Man-Computer Graphics/MCG/ allows operator control through oscilloscope via light sensitive pen). *Astronautics and Aeronautics*, 4, 58-62.
- Gray A., (1997). *Modern Differential Geometry of Curves and Surfaces with Mathematica*, 2nd ed. Boca Raton, FL: CRC Press, p. 292.
- Hein, P. 2021. "Piet Hein" <https://piethein.com/piet-hein/>
- Hwang, C. O., & Mascagni, M. (2004). Electrical capacitance of the unit cube. *Journal of applied physics*, 95(7), 3798-3802.
- Jaklic, A., Leonardis, A., & Solina, F. (2000). Superquadrics and their geometric properties. In *Segmentation and recovery of superquadrics* (pp. 13-39). Springer, Dordrecht.
- Jo, Y. H., Cheon, C., Park, H., Hur, M. Y., & Lee, H. J. (2022). Multi-dimensional electrostatic plasma simulations using the particle-in-cell method for the low-temperature plasmas for materials processing. *Journal of the Korean Physical Society*, 1-12.
- Khatib, O. (1985). Real-time obstacle avoidance for manipulators and mobile robots. In *Proceedings. 1985 IEEE International Conference on Robotics and Automation* (Vol. 2, pp. 500-505). IEEE.

- Maas, L. R. (1994). On the surface area of an ellipsoid and related integrals of elliptic integrals. *Journal of Computational and applied mathematics*, 51(2), 237-249.
- Mac Huang, J., Shelley, M. J., & Stein, D. B. (2021). A stable and accurate scheme for solving the Stefan problem coupled with natural convection using the Immersed Boundary Smooth Extension method. *Journal of Computational Physics*, 432, 110162.
- Magalhaes, H., Marques, F., Liu, B., Antunes, P., Pombo, J., Ambrosio, J., Piotrowski, J., Bruni, S. (2020). Implementation of a non-Hertzian contact model for railway dynamic application. *Multibody Syst. Dyn.* 48(1), 41–78.
- Maplesoft (2021). Superellipsoid - Maple Help. <https://www.maplesoft.com/support/help/maple/view.aspx?path=MathApps%2FSuperellipsoid>
- Michon G.P. (2020). Spheroids & Scalene Ellipsoids. <http://www.numericana.com/answer/ellipsoid.htm>
- Nagornov, K. O., Kozhinov, A. N., & Tsybin, Y. O. (2021). Spatially-distributed cyclotron oscillators approach to FT-ICR MS at the true cyclotron frequency: Computational evaluation of sensitivity. *International Journal of Mass Spectrometry*, 466, 116604.
- Ruehli, A. E., & Brennan, P. A. (1973). Efficient capacitance calculations for three-dimensional multiconductor systems. *IEEE Transactions on microwave Theory and Techniques*, 21(2), 76-82.
- Sedaghat, M. H., Bagheri, A. A. H., Shahmardan, M. M., Norouzi, M., Khoo, B. C., & Jayathilake, P. (2021). A hybrid immersed boundary-lattice Boltzmann method for simulation of viscoelastic fluid flows interaction with complex boundaries. *Commun Comput Phys*, 29(5), 1411-1445.

- Silvia, P. J., & Barona, C. M. (2009). Do people prefer curved objects? Angularity, expertise, and aesthetic preference. *Empirical studies of the arts*, 27(1), 25-42.
- Sun, K., Ding, S., Zhang, J., & Liu, Y. C. (2022). Solving the Eigenfrequencies Problem of Waveguides by Localized Method of Fundamental Solutions with External Source. *Mathematics*, 10(7), 1128.
- Suresh, N., Nithyadevi, N., & Chamkha, A. J. (2022). Natural convection of alumina-water nanofluid in a partially heated square cavity with isothermal blockage inside with uniform magnetic field and heat generation/absorption. *The European Physical Journal Plus*, 137(3), 1-15.
- Talu S. D. L. (2011). "Complex 3D Shapes with Superellipsoids, Supertoroids and Convex Polyhedrons," *Journal of Engineering Studies and Research*, vol. 17, no. 4, pp. 96–100.
- Uckermann A., Haschke R., and Ritter H. (2012). "Real-time 3D segmentation of cluttered scenes for robot grasping," *IEEE-RAS International Conference on Humanoid Robots*, pp. 198–203.
- Varadarajan K. M. and Vincze M. (2011). "Affordance based Part Recognition for Grasping and Manipulation," *ICRA Workshop on Autonomous Grasping*, no. April.
- Volpe, R., & Khosla, P. (1990). Manipulator control with superquadric artificial potential functions: Theory and experiments. *IEEE Transactions on Systems, Man, and Cybernetics*, 20(6), 1423-1436.
- Warnapala, Y., & Dinh, H. (2013). Numerical solution of the helmholtz equation for the superellipsoid via the galerkin method. *Communications in Numerical Analysis*, 2013, I-12.
- Weisstein, Eric W. (2021b)."Superellipse." From MathWorld--A Wolfram Web Resource. <https://mathworld.wolfram.com/Superellipse.html>

- Weisstein, Eric W. (2021a). "Superellipsoid." From MathWorld--A Wolfram Web Resource. <https://mathworld.wolfram.com/Superellipsoid.html>
- Westerman, S. J., Gardner, P. H., Sutherland, E. J., White, T., Jordan, K., Watts, D., & Wells, S. (2012). Product design: Preference for rounded versus angular design elements. *Psychology & Marketing*, 29(8), 595-605.
- Wintle, H. J. (2004). The capacitance of the cube and square plate by random walk methods. *Journal of electrostatics*, 62(1), 51-62.



**CHAPTER 4**

**GEANT4 SIMULATION OF THE EFFECT OF  
TRAPEZOIDAL AND RECTANGULAR CRYSTAL  
SHAPES ON THE TRANSMISSION OF LYSO: Ce  
EMISSION PHOTONS**

Dr. Öğr. Üyesi Adnan KILIÇ<sup>1</sup>

---

<sup>1</sup>Bursa Uludağ University, Science & Art Faculty, Department of Physics, Bursa, Turkey.  
adnank@uludag.edu.tr <https://orcid.org/0000-0003-0983-7504>



## INTRODUCTION

Inorganic crystals are widely used materials for radiation detection in fields such as high energy physics (HEP) experiments, space, astrophysics, and medical imaging (PET). Energy transferred to the crystal during the passage of a radiation is converted into light through the process of scintillation. These photons are converted into an electrical signal, usually by a photo-detector attached to the tip of the crystal.

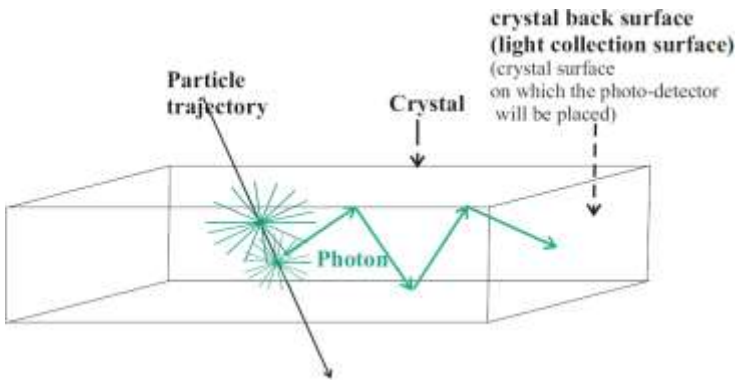


**Figure 1:** A Representative Picture Of Scintillation Photon Generation And Tracking In A Inorganic Crystal

There are many inorganic crystals that are likely to be used in high energy detectors. Limitations such as the type of radiation to be detected and the place where the crystal will be used affect the crystal selection. Crystal selection is made by looking at a few important parameters such as intensity, light product, scintillation kinetics, emission spectrum, radiation hardness. Durability, moisture absorption and production cost are also very important parameters (Fabjan et al., 2020). Some crystals commonly used in high energy physics experiments and their properties are given in Table 1 (Mao et al, 2008). Cerium doped lutetium yttrium oxy-orthosilicate ( $\text{Lu}_{2x}\text{Y}_{2-2x}\text{SiO}_5:\text{Ce}$ ,

LYSO:Ce) crystal has high light output, fast scintillation response, high density, good energy resolution and also high radiation hardness as can be seen from Table 1. The superior qualities of the LYSO:Ce crystal compared to other inorganic crystals have enabled it to be used in today's particle physics experiments (such as SuperB, KOLE and Mu2e) (Mao et al., 2011). It has also made it a candidate for electromagnetic calorimeter of the compact muon solenoid detector (CMS) in the high luminosity large hadron collider (HL-LHC) planned for the future.

**Table 1:** Properties of Some Commonly Used Scintillation Crystals

Crystal	NaI:Tl	CsI:Tl	CsI:Na	CsI	BaF <sub>2</sub>	CeF <sub>3</sub>	BGO	PWO:Y	LSO/LYSO
Density (g/cm <sup>3</sup> )	3.67	4.51	4.51	4.51	4.89	6.16	7.13	8.3	7.40
Melting Point (°C)	651	621	621	621	1280	1460	1050	1123	2050
Radiation Length (cm)	2.59	1.86	1.86	1.86	2.03	1.70	1.12	0.89	1.14
Molière Radius (cm)	4.13	3.57	3.57	3.57	3.10	2.41	2.23	2.00	2.07
Interaction Length (cm)	42.9	39.3	39.3	39.3	30.7	23.2	22.8	20.7	20.9
Refractive Index <sup>a</sup>	1.85	1.79	1.84	1.95	1.50	1.62	2.15	2.20	1.82
Hygroscopicity	Yes	Slight	Yes	Slight	No	No	No	No	No
Luminescence <sup>b</sup> (nm)	410	550	420	420	300	340	480	425	402
(at Peak)				310	220	300		420	
Decay Time <sup>b</sup> (ns)	245	1220	690	30	650	30	300	30	40
				6	0.9			10	
Light Yield <sup>b,c</sup>	100	165	88	3.6	36	7.3	21	0.30	85
				1.1	4.1			0.077	
dLY/dT <sup>b,d</sup> (%/°C)	-0.2	0.4	0.4	-1.4	-1.9	~0	-0.9	-2.5	-0.2
					0.1				

<sup>a</sup> At the wavelength of the emission maximum.

<sup>b</sup> Top line: slow component, bottom line: fast component.

<sup>c</sup> Relative light output with QE of the readout device taken out for samples of 1.5 X<sub>0</sub>.

<sup>d</sup> At room temperature (20°C).

Optical photon tracking simulations are a common method used in detector designs to achieve optimal scintillator geometry, scintillator surface, and greatest light collection efficiency (Roncali et al., 2017; Blackberg et al., 2018; Chen et al., 2013; Hong et al., 2011; Leming et al., 2013; Knyazev et al., 2021). For good energy resolution in scintillation detectors, it is desired that a very large number of photons are released in the crystal and that they are transmitted to the photo-

detector with as little loss as possible. Light collection efficiency (the fraction of photons generated by the scintillation process that reaches the photo-detector) has always been an important parameter in the optimization of scintillation detectors (Danevich et al., 2014). In this section, in accordance with the emission spectrum of a LYSO:Ce crystal, optical photons produced with random energies at different positions in trapezoidal and rectangular crystals were tracked via GEANT4 Monte Carlo tool. Depending on the optical photon energy and emission position, the rate at which they reach the light collection surface for both crystal shapes was investigated separately. Considering both crystal shapes, the effect of crystal geometry on the rate of photons reaching the collection surface was expressed with quantitative results.

## 1. SIMULATION

GEANT4 (Geometry and Tracking) is an object-oriented simulation tool written in C++ that can transport many different types of particles in a variety of environments at a microscopic scale. It was originally developed by CERN for high energy physics applications, and today it has application in many different fields. Geant4 provides hadronic, electromagnetic and optical physics processes over a wide energy range and for many particle types. In addition, it provides tracking and visualization and geometry definitions suitable for fields such as high energy, nuclear, astrophysics, medicine and space science (Agostinelli et al, 2003). In this study, version 10.0 of GEANT4 was used for simulations. The ROOT analysis program, an open-source data processing system created at CERN, was used to analyze the GEANT4 data. The data generated during GEANT4 simulation is transferred to ROOT files via C++ objects. The transferred data is then converted into histograms or graphs via macro files, which are a series of user-prepared C++ scripts. The volumes of data produced with GEANT4 can be very large. ROOT is also an extremely useful tool for quick

access to large volumes of data (Brun et al., 1997). ROOT program was used to produce graphics.

### **1.1 Optical Photon Physics Processes**

In GEANT4, an optical photon is treated like a normal particle with partial wave properties, as it can undergo refraction and reflection with wavelengths longer than the atomic space created by scintillation processes. A charged particle loses energy as it passes through the crystal, during this time, the stored energy in the crystal is converted into randomly polarized optical photons. A optical photon can undergo Rayleigh scattering, MIE scattering, bulk absorption in the bulk material and reflection, refraction and absorption interactions on the boundary surface. Rayleigh scattering is the process of elastic scattering of light by medium particles smaller than their wavelength and a very unlikely process for optical photons. MIE scattering is based on the analytical solution of Maxwell's equations for optical photons scattering from spherical particles and only important when the radius of the scattering object is order of wavelength. Bulk absorption is the absorption of an optical photon by the molecules of a bulk material (Geant4 Collaboration, 2013). It is a very important process in optical photon tracking, as it will cause a decrease in the number and energy of optical photons generating the signal in the photo-detector. In GEANT4, the possible physics processes that an optical photon will undergo when it comes to a boundary surface vary depending on the properties of the boundary surface. This parameter is called surface finish. There are two boundary surface models in GEANT4: the GLISUR and the UNIFIED model. The GLISUR model has only two surface finish variants: polished and ground. In the UNIFIED model, a more realistic simulation model is provided in every aspect in terms of surface finish and reflector coating for dielectric-dielectric boundary surfaces. Two materials separated by a boundary can be dielectric-dielectric or dielectric-metal. Surface finish types for dielectric-

dielectric are polished and ground. If the dielectric-dielectric boundary surface is polished, Snell's law is applied according to the refractive index of the two materials, but before that reflectivity is used to determine whether the photon will be absorbed or not. If the photon encounters a ground surface, reflectivity is used to determine whether the photon will be absorbed or not, then a micro facet is selected according to a  $\sigma_\alpha$  parameter in the first step. The angle  $\alpha$  between the average boundary surface normal and the selected micro surface normal shows a gaussian distribution. The parameter  $\sigma_\alpha$  is the standard deviation of this gaussian distribution. According to this facet normal, Snell's law is applied. If Snell's law results in reflection, one of four types of reflection will occur according to the probabilities assigned: Specular spike, specular lobe, backscatter and lambertian.

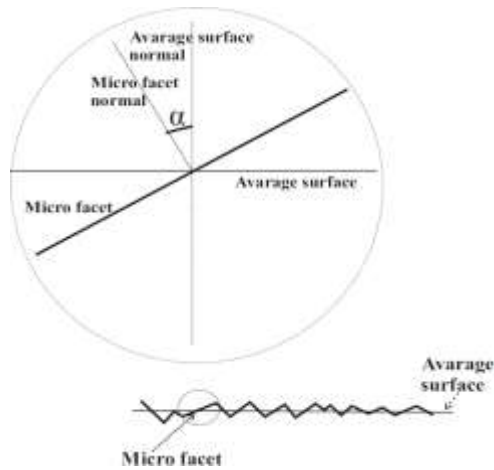


**Figure 2:** A Ground Surface Composed Of Micro-Facets.  $\alpha$  is The Angle Between The Average Surface And The Micro-Facet Normals (adapted from (Kandemir, 2018)).

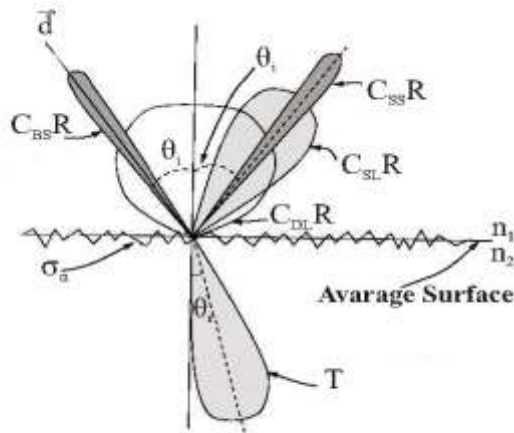


**Figure 3:** Polar Graphic Of Radiant Flux Per Unit Solid Angle For The UNIFIED Model (adapted from (Papacz, 2010)).

$C_{SL}R$  (Specular lobe constant) : reflection probability relative to a micro facet normal.  $C_{SS}R$  (Specular spike constant) : probability of reflection with respect to the average surface normal.  $C_{DL}R$  (Diffuse lobe constant) : Lambertian inner reflection probability.  $C_{BS}R$  (Backscatter spike constant) : several reflections within a deep groove with the ultimate result exact back-scattering.

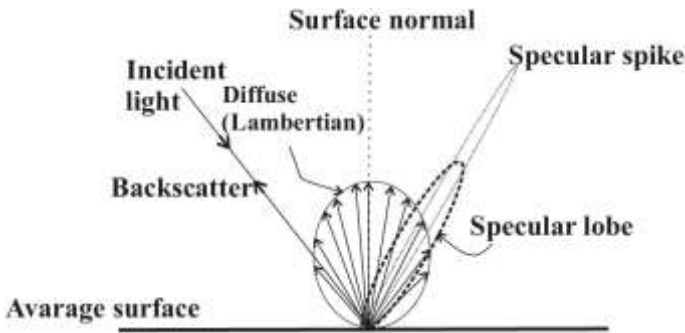


**Figure 4:** Light Reflection Types Available For The Ground Surface In GEANT4: Specular Spike (i.e., Perfect Mirror), Specular Lobe, And Diffuse (Lambertian) (adapted from (Cuplov, 2014)).

It is also possible to define coating types on the dielectric-dielectric surface, which represent a special reflector with a given reflectivity coefficient. If a scintillator surface is perfectly coated with a

reflector, it is called front painted. On the other hand, if a imperfect reflector coating is applied on the scintillator so that an air gap remains between the scintillator and the reflector, it is called black painted. In the Unified model, reflector coating surface types are supplied as polishedbackpainted, polishedfrontpainted, groundbackpainted and groundfrontpainted. Snell's law involves using Fresnel's equations for reflection and refraction. As a result of applying Snell's law and Fresnel's equations together, Fresnel refraction, total internal reflection or Fresnel reflection can occur (Allison et al, 2013).

### **1.2 Simulation Details**

By means of GEANT4, LYSO:Ce emission photons (optical photon) were tracked in a rectangular and trapezoidal LYSO:Ce crystals. The general particle source (GPS), part of GEANT4, allows the spectrally spatial and angular distributions of the primary particle source to be defined in a macro file as command lines. In the simulation, optical photons are not produced by scintillation processes. They were produced according to the emission spectrum of LYSO:Ce crystal and used as primary particles by means of GPS. In the simulation, only optical photon tracking was done in the crystal. Interactions of the optical photon with the medium or the boundary surface are included in the simulation via the G4OpticalPhysics class. All processes that the optical photon can undergo are included in this physics class. Optical photons are produced at different positions in the crystal, with random linear polarity and in the direction of momentum pointing to the crystal back surface. These optical photons are reflected from the crystal side surfaces and travel towards the light collection surface of the crystal (see Figure 1). As soon as the primary optical photon reaches this surface, the energy of the photon is recorded and counted. Immediately after, its tracking is terminated. For both crystal geometries, the number of photons collected and their energy distributions are estimated as a function of the distance between the

position where the primary optical photons are emitted and the light collection surface. In the simulations, 25x25x200 mm rectangular (Zhang et al, 2008) and 20x23x200 mm trapezoidal (Yang et al, 2015) crystal geometries were considered. In order to obtain more accurate results, the optical components such as refractive index and absorption length as a function of photon energy to be assigned to the crystal must be precisely defined in simulation. In addition, the properties of the boundary surface connecting two different materials should also be defined. Some of the mentioned optical quantities (refractive index (Mao et al, 2008) and absorption length (Vilardi et al, 2006)) used in the simulation were taken from the literature. Absorption length (ABSLENGTH) is average distance the optical photon will travel before it is absorbed in bulk material. At the end of this distance, the process kills the photon. The surface properties used in the GEANT4 simulation are given in Table 2:

**Table 2:** Surface Definitions Used In GEANT4 Simulation

<b>Name</b>	<b>LYSO:Ce-Air</b>
surface model	UNIFIED
surface type	dielectric-dielectric
surface finish	groundbackpainted
$\sigma_g$	0.1
refractive index of the intermediate layer between the surfaces	1.0
$C_{SL}$	1
$C_{SS}$	0
$C_{BS}$	0
reflectivity	1

Figure 5 shows the simulation images of the trajectories of 1 optical photon (top picture) and 100 optical photons (bottom picture) in a rectangular and trapezoidal LYSO:Ce crystal, obtained with DAWN event visualization program (Tanaka, 1997) in GEANT4.

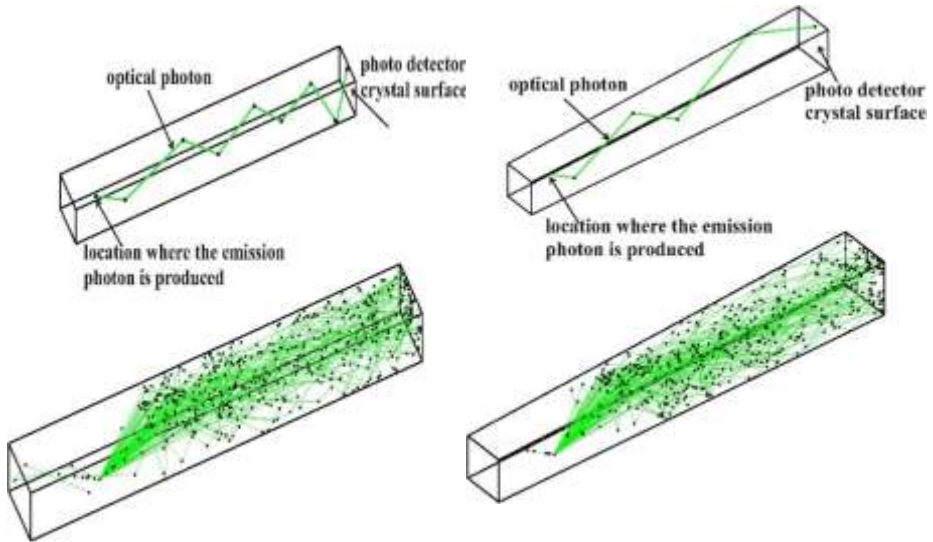


**Figure 5:** Tracking Images Produced With DAWN Of Emission Optical Photons In The Crystal For Rectangular (Left) And Trapezoidal Shape (Right)

## 2.SIMULATION RESULTS

The energy distributions of fraction of what reaches the light collection surface of LYSO:Ce emission photons emitted at different positions in rectangular and trapezoidal crystals can be seen in Figure 6.

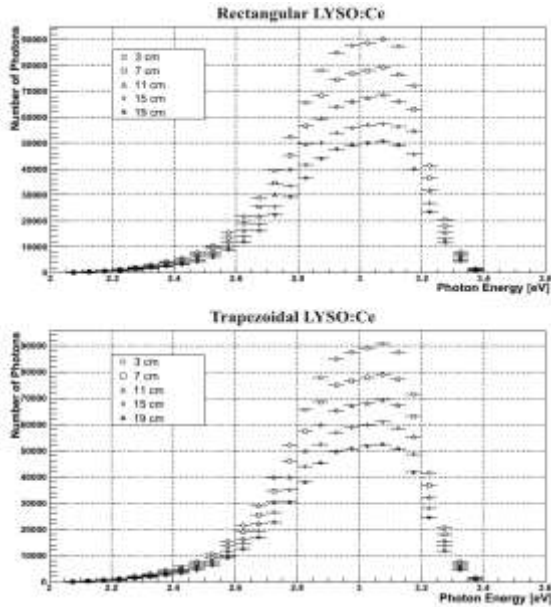


**Figure 6:** Photon Energy Distributions On Collection Surface For Photon Emission Positions At Different Distances (Top: Rectangular, Bottom: Trapezoidal)

Since the surface definitions given in Table 2 are used in the simulation, the optical photon travels through the crystal by making reflection, refraction or total internal reflection and is absorbed in the crystal according to the absorption lengths provided by the user (bulk absorption). As can be seen in Figure 6, optical photon loss for both crystal geometries increases significantly with distance from the light collection surface. It was determined that there was a photon loss of 3% to 49% over all photon energies in rectangular crystals and 3% to 47% in trapezoidal crystals. It has been observed that the only cause of optical photon loss in the simulation is bulk absorption.

Figure 7 and Figure 8 show that optical photons reaching the collection surface are compared with the initially emitted photons at different positions in the rectangular and trapezoidal crystals.

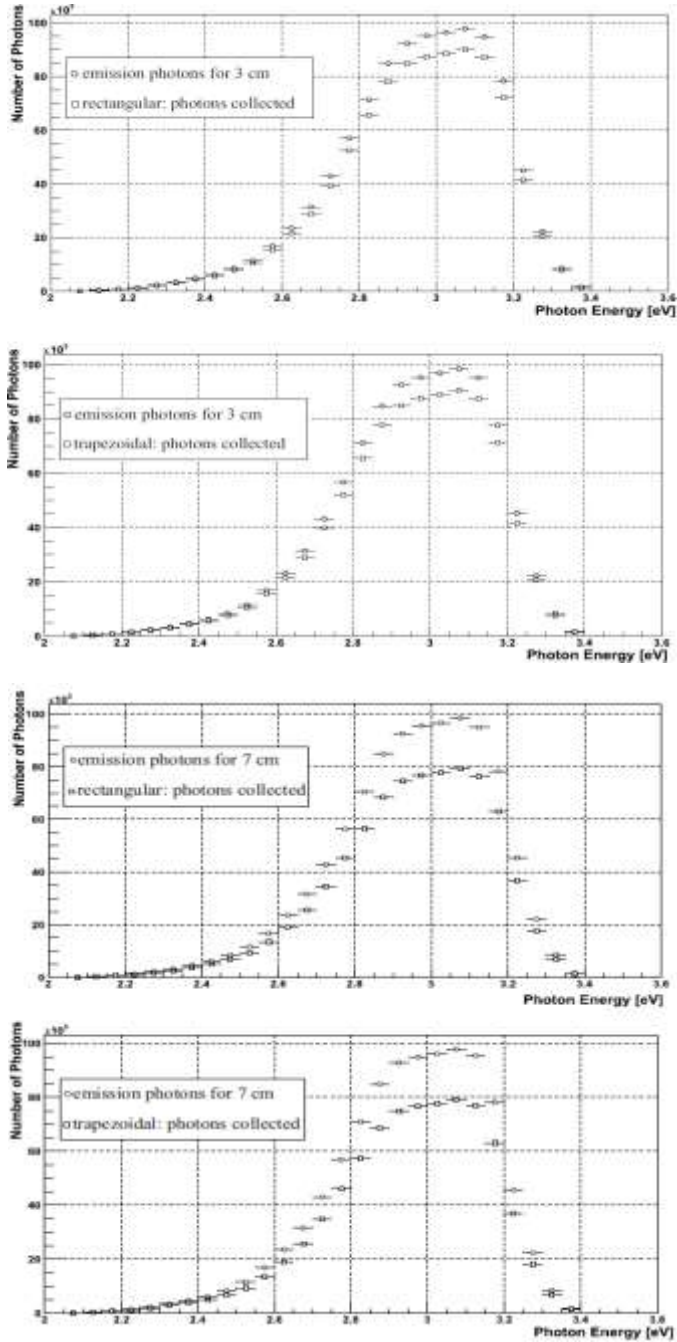


**Figure 7:** The Emission And Collected Photon Energy Distributions For Distances Of 3 cm and 7 cm From Collection Surface For Rectangular And Trapezoidal LYSO:Ce Crystals

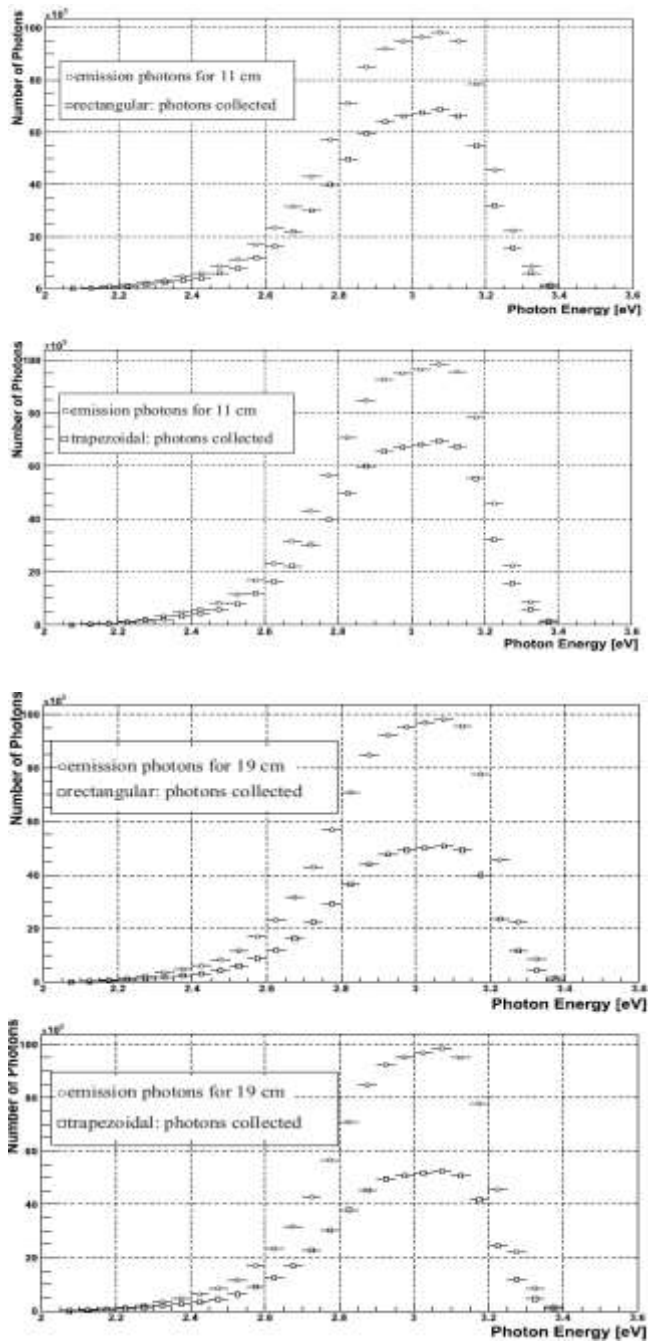


**Figure 8:** The Emission And Collected Photon Energy Distributions For Distances Of 11 cm and 19 cm From Collection Surface For Rectangular And Trapezoidal LYSO:Ce Crystals

As can be seen from Figure 7 and Figure 8, the number of photons collected decreases significantly with distance from the collection surface for both crystal shapes.

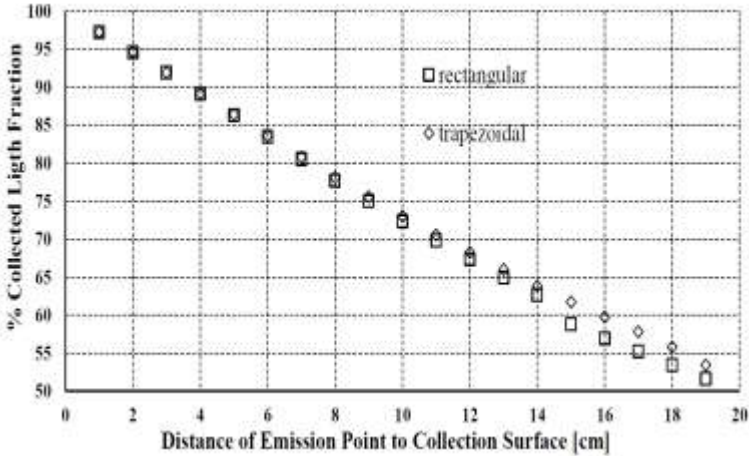


**Figure 9:** Variation Of The Amount Of Light Collected With The Distance Of Emission Position From Collection surface For Rectangular And Trapezoidal LYSO:Ce Crystals

From Figure 9, it can be seen that while there is no significant difference in photon collection in both crystal shapes for emissions close to the light collection surface, there is an improvement at the rate of photons collected for the trapezoidal crystal compared to the rectangular shape as it moves away from the collection surface.

## CONCLUSION

There are different companies producing crystals (e.g such as Shanghai Institute of Ceramics, Saint-Gobain Corporation, Sichuan Institute of Piezoelectric and Acousto-optic Technology). Depending on the crystal growth technique and Y and Ce concentrations, LYSO:Ce crystals with the same geometric shape and dimensions may show different optical properties from each other. Also, wrapping, coating and roughing of the crystal surface can cause a change in the refractive indices. In this work, GEANT4 simulation of optical photon transport in 20x23x200 mm trapezoidal and 25x25x200 mm

rectangular shape LYSO:Ce crystals has been made. The findings obtained in the simulation are for the optical properties taken from the literature and the surface properties given in Table 2. The crystal is not covered with any material. Photo-detector and signal generation are also not simulated. The obtained results showed that the optical photon loss per unit length of LYSO:Ce crystal was about 2.71% for the rectangular and 2.64% for the trapezoidal over all emission photon energies. It is predicted that there will be approximately 0.01% to 2.95% more loss in light collected in the rectangular than in the trapezoidal for selected crystal dimensions.

## REFERENCES

- Agostinelli S. et al (2003). GEANT4—a simulation toolkit Nucl. Instrum. Methods Phys. Res. A 506 50–303.
- Allison et al ( Geant4 Collaboration ) (2013). Geant4 User’s Guide for Application Developers Version: Geant4.10.0 <http://www.geant4.org/>
- Blackberg, L., El Fakhri G., Sabet, H. (2018). Simulation study of light transport in laser-processed LYSO:Ce detectors with single-side readout Phys Med Biol. 62(21): 8419–8440.
- Brun R., Rademakers F. (1997). ROOT - An Object Oriented Data Analysis Framework, Proceedings AIHENP’96 Workshop, Lausanne, Sep. 1996, Nucl. Inst. & Meth. in Phys. Res. A 389 81-86. See also <https://root.cern/>
- Chen, Z. et al (2013). Optimum performance investigation of LYSO crystal pixels: A comparison between GATE 2 simulation and experimental data arXiv:1309.3736v1.
- Cuplov, V., Buvat, I., Pain, F., Jan, S. (2014). Extension of the GATE Monte-Carlo simulation package to model bioluminescence and fluorescence imaging Journal of Biomedical Optics doi: 10.1117/1.JBO.19.2.026004
- Danevich, F. A., Kobychiev V. V., Kobychiev, R. V., Kraus, H., Mikhailik, V. B., Mokina, V. M., Solsky, I. M. (2014). Impact of geometry on light collection efficiency of scintillation detectors for cryogenic rare event searches Nuclear Instruments and Methods in Physics Research B 336 26–30.
- Geant4 Collaboration (2013) Geant4 Physics Reference Manual Version: Geant4 10.0 <http://www.geant4.org/>
- Hong, S. J. et al (2011). A Feasibility Study on the Use of Optical Fibers for the Transfer of Scintillation Light to Silicon Photomultipliers IEEE Transactions On Nuclear Science Vol. 58, No. 3.
- Kandemir, M., Çakır, A. (2018). Simulation and Efficiency Studies of Optical Photon Transportation and Detection with Plastic

- Antineutrino Detector Modules Nuclear Inst. and Methods in Physics Research, A 898 30–39.
- Knyazev, A. et al (2021). Simulations of light collection in long tapered CsI(Tl) scintillators using real crystal surface data and comparisons to measurement Nuclear Inst. and Methods in Physics Research, A 1003 165302.
- Leming, E., De Santo, A., Salvatore, F., Camanzi, B., Lohstroh, A. (2014). A GEANT4 Monte Carlo simulation to describe the time response of a coupled SiPM and LYSO detection system Journal of Instrumentation 9 C06008.
- Mao, R., Zhang L., Zhu, R. Y. (2011). LSO/LYSO Crystals for Future HEP Experiments Journal of Physics: Conference Series 293 012004.
- Mao, R., Zhang, L., Zhu, R. Y. (2008). Emission Spectra of LSO and LYSO Crystals Excited by UV Light, X-Ray and  $\gamma$ -ray IEEE Transactions On Nuclear Science Vol. 55, No. 3
- Papacz, P. (2010). Optimisation of the Particle Detection Efficiency for Scintillation Detectors with SiPM Readout Diploma thesis. RWTH Aachen, [http://web.physik.rwth-aachen.de/~hebbeker/theses/papacz\\_diploma.pdf](http://web.physik.rwth-aachen.de/~hebbeker/theses/papacz_diploma.pdf) (cit. on pp. 40, 41, 43, 52, 202).
- Roncali, E., Stockhoff, M., Cherry, S. R. (2017). An integrated model of scintillator-reflector properties for advanced simulations of optical transport Phys Med Biol. 62(12): 4811–4830.
- Tanaka S., Kawaguti, M. (1997). DAWN for Geant4 Visualization, Proceedings of the CHEP '97 Conference, Berlin (Germany). For documentation, see [http://geant4.kek.jp/~tanaka/DAWN/About\\_DAWN.html](http://geant4.kek.jp/~tanaka/DAWN/About_DAWN.html).
- Vilardi, I., et al (2006). Optimization of the effective light attenuation length of YAP:Ce and LYSO:Ce crystals for a novel geometrical PETconcept 564, 1 ,506-514.
- Vol. 898, 30-39 <https://doi.org/10.1016/j.nima.2018.04.059>

Yang, F., Mao, R., Zhang L., Zhu, R.Y. (2015). Characterization of Three LYSO Crystal Batches Journal of Physics Conference Series 587 012065.



## CHAPTER 5

### FUZZY PARAMETERIZED INTUITIONISTIC FUZZY SOFT TOPOLOGY AND ITS APPLICATION TO DECISION- MAKING

Asst. Prof. Adem YOLCU<sup>1</sup>  
Assoc. Prof. Taha Yasin ÖZTÜRK<sup>2,3</sup>

---

<sup>1</sup> Department of Mathematics, Kafkas University, Kars, Turkey, E-mail:  
[yolcu.adem@gmail.com](mailto:yolcu.adem@gmail.com), Orcid.: 0000-0002-4317-652X

<sup>2</sup> Department of Mathematics, Kafkas University, Kars, Turkey, E-mail:  
[taha36100@hotmail.com](mailto:taha36100@hotmail.com), Orcid.: 0000-0003-2402-6507

<sup>3</sup> A part of this chapter was presented as a abstract paper at the 4th International Conference on  
Mathematical and Related Sciences 2021.



## INTRODUCTION

We all know that the actual world is replete of uncertainty, inaccuracy, and ambiguity. In reality, the majority of the issues we dealt with were ambiguous rather than specific. Classical approaches are not always successful when confronted with so much uncertain data; this is due to the numerous sorts of uncertainty prevalent in these issues. It is commonly recognized that probabilistic theories, fuzzy sets (Zadeh, 1965), intuitionistic fuzzy sets (Atanassov,1986), rough sets (Zhan et.al, 2015), and other mathematical theories are frequently appropriate techniques to describing uncertainty. However, as Molodtsov pointed out, each of these hypotheses has its own set of problems. To address these issues, Molodtsov introduced a novel way to modeling uncertainty known as a soft set (Molodtsov, 1999). This theory is now used in many fields, including information sciences, intelligent systems, function smoothness, game theory, measurement theory, probability theory and so on. Many theorists have improved the principle by extending it to topological spaces (Cagman et.al., 2011; Shabir and Naz 2011; Zhan et.al., 2015), category theory, ring theory (Acar et.al.,2010; Aktas and Cagman,2007; Celik and Ekiz, 2011), and decision-making problems (Cagman and Enginoglu, 2010; Chen et.al., 2005; Maji et.al., 2002). Researchers have combined fuzzy set and soft set to broaden the spaces and tackle increasingly difficult issues. In this approach, several intriguing applications of soft set theory have been extended. As the first hybrid of a fuzzy set and a soft set, Maji et al. (Maji et.al., 2001) proposed the fuzzy soft set. Fuzzy soft set theory has been developed in a variety of ways (Feng et.al., 2010; Kong et.al. 2009; Roy and Maji, 2007) in terms of topology (Atanassov,1986; Simsekler and Yuksel, 2013), different algebraic structures (Aygunoglu and Aygun, 2009; İnan and Ozturk, 2012), and, in particular, decisionmaking. Cagman et al. (Cagman and Enginoglu, 2010) proposed a second combination of fuzzy set and soft set, dubbed fuzzy parametrized soft set (as shortly FPS set). Cagman et al. presented

operations on FPS sets and enhanced various conclusions in that study. Following that, Cagman and Deli (Cagman and Deli, 2012) used FPS sets to explain decision-making strategies, which they subsequently extended to situations including complexity and fuzzy objects. Cagman et al. (Cagman et.al., 2010) developed a third and final one, dubbed fuzzy parametrized fuzzy soft set. Then, by defining operations on FPFS sets, they enhanced a strategy for tackling particular decision-making issues. Zorlutuna and Atmaca (Zorlutuna and Atmaca, 2016) present the topological structure of fuzzyfying soft sets, known as fuzzy parametrized fuzzy soft sets. They also looked at the fundamental aspects of the concept of quasi-coincidence for fuzzy parametrized fuzzy soft sets. Riaz and Hashmi (Riaz and Hashmi, 2017) looked at the concept of fuzzifying soft sets, also known as fuzzy parameterized fuzzy soft sets (FPFS-sets), as well as some conclusions that are valid in crisp set theory but not in FPFS-set. They added closure, interior, border, and exterior to the idea of FPFS-topological places. They also discuss the FPFS-sets' quasi-coincidence and Q-neighborhood features. In 2019, The notion of fuzzy parameterized intuitionistic fuzzy soft sets is proposed by Sulukan et al. (FPIFS-sets) (Sulukan et.al., 2019). They apply these sets to a performance-based value assignment (PVA) problem and make research recommendations.

## 1. PRELIMINARIES

**Definition 1.1** A pair  $(G, E)$  is called a soft set over  $R$  if it is a mapping defined by  $G: E \rightarrow P(R)$ . In the other words, a soft set is a parameterized family of subsets of the set  $R$ . For each  $\alpha \in E$ , the set  $G(\alpha)$  may be considered as the set of  $\alpha$ -elements of the soft set  $(G, E)$  (Molodtsov, 1999).

**Definition 1.2** Let  $R$  be an initial universe. A fuzzy set  $F$  in  $R$ ,  $F = \{(s, \mu_F(s)) : s \in R\}$ , where  $\mu_F: R \rightarrow [0, 1]$  is the membership

function of the fuzzy set  $F$ . The set of all fuzzy sets over  $R$  will be denoted by  $FP(U)$ . (Zadeh, 1965).

**Definition 1.3** Let  $R$  be an initial universe,  $E$  be a set of parameters and  $FP(R)$  be the set of all fuzzy sets in  $R$ . Then a pair  $(F, E)$  is called a fuzzy soft set over  $R$ , where  $F : E \rightarrow FP(R)$ . (Maji et.al., 2001).

**Definition 1.4** Let  $R$  be an initial universe. An intuitionistic fuzzy (IF) set  $G$  over  $R$  is defined by

$$G = \{(\mu(s), \nu(s) / s : s \in R\}$$

where  $\mu : R \rightarrow [0,1]$  and  $\nu : R \rightarrow [0,1]$  such that  $0 \leq \mu(s) + \nu(s) \leq 1$  for all  $s \in R$ . (Atanassov, 1986).

**Definition 1.5** Let  $R$  be a universal set and  $E$  be a set of attributes. If  $U = \{(s, \mu_U(s)) : s \in R\}$  is a fuzzy set over  $R$ . Then fuzzy parameterized intuitionistic fuzzy soft (FPIFS) set over  $R$  defined by

$$G_U = \{(\mu_U(y) / y, \{\mu(s), \nu(s) / s\}) : y \in E, s \in R\}$$

then  $G_U$  called an FPIFS set over  $R$ . The set of all FPIFS sets over  $R$  is denoted by  $FPIFS(G_{\tilde{R}})$  (Sulukan et.al., 2019).

**Definition 1.6** Let  $G_U$  be a FPIFS set over  $R$ .

If  $\mu_U(y) = 0$  and  $G = \{(0,1) / s_i : s_i \in R\}$  then  $G_U$  is called a null FPIFS set and denoted by  $G_{\emptyset}$ .

If  $\mu_U(y) = 1$  and  $G = \{(1,0) / s_i : s_i \in R\}$  then  $G_U$  is called a absolute FPIFS set and denoted by  $G_{\tilde{R}}$ . (Sulukan et.al., 2019).

**Definition 1.7** Let  $G_U, G_V \in FPIFS(G_{\tilde{R}})$ . Then

1.  $G_U$  is called FPIFS subset of  $G_V$ , denoted by  $G_U \underline{\subseteq} G_V$ , if  $\mu_U(y) \leq \mu_V(y)$  and  $U \subseteq V \quad \forall y \in E$ .
2. The union of two FPIFS sets  $G_U$  and  $G_V$  is denoted by  $G_U \tilde{\cup} G_V$  and defined by
3.  $G_U \tilde{\cup} G_V = \{(\max(\mu_U(y), \mu_V(y)) / y, G_U(s) \cup G_V(s) : s \in R)\}$
4. The intersection of two FPIFS sets  $G_U$  and  $G_V$  is denoted by  $G_U \tilde{\cap} G_V$  and defined by
5.  $G_U \tilde{\cap} G_V = \{(\min(\mu_U(y), \mu_V(y)) / y, G_U(s) \cap G_V(s) : s \in R)\}$
6. The complement of  $G_U$  is denoted by  $G_U^c$  and defined by
7.  $G_U^c = \{((1 - \mu_U(y)) / y, \{v(s), \mu(s) / s\}) : y \in E, s \in R\}$
8. (Sulukan et.al., 2019).

## 2. MAIN RESULTS

**Definition 2.1** A FPIFS topological space is a pair  $(R, \tilde{\tau})$  where  $R$  is a non-empty set and  $\tilde{\tau}$  is a family of FPIFS sets over  $R$  satisfying the following properties:

- i.  $G_\emptyset, G_{\tilde{R}} \in \tilde{\tau}$ ,
- ii. If  $G_U, G_V \in \tilde{\tau}$ , then  $H_U \tilde{\cap} H_V \in \tilde{\tau}$ ,
- iii. If  $G_{U_i} \in \tilde{\tau}, \forall i \in I$ , then  $\bigcup_{i \in I} G_{U_i} \in \tilde{\tau}$

Then  $\tilde{\tau}$  is called a FPIFS-topology on  $R$ . Every member of  $\tilde{\tau}$  is called FPIFS-open set in  $(R, \tilde{\tau})$ .  $G_U$  is called a FPIFS-closed set in  $(R, \tilde{\tau})$  if  $(G_U)^c \in \tilde{\tau}$ .

**Example 2.1** The family  $\tilde{\tau} = \{G_\emptyset, G_U\}$  is indiscrete FPIFS topology on  $R$  and the family  $FPIFS(G_{\bar{R}})$  is indiscrete FPIFS topology on  $R$ .

**Example 2.2** Let  $R = \{s_1, s_2, s_3\}$  be the set of universe and let  $E = \{y_1, y_2, y_3, y_4\}$  be the set of attributes. If  $U = \{0.2 / y_1, 0.6 / y_2, 0.7 / y_4\} \subseteq E$ ,  $V = \{0.1 / y_1, 0.6 / y_4\}$  with FPIFS sets,

$$G_U = \left\{ \begin{array}{l} (0.2 / y_1, \{(0.2, 0.3) / s_1, (0.3, 0.5) / s_2, (0.8, 0.2) / s_3\}), \\ (0.6 / y_2, \{(0.5, 0.4) / s_1, (0.6, 0.3) / s_2, (0.3, 0.5) / s_3\}), \\ (0.7 / y_4, \{(0.2, 0.4) / s_1, (0.4, 0.4) / s_2, (0.2, 0.6) / s_3\}) \end{array} \right\}$$

and

$$G_V = \left\{ \begin{array}{l} (0.1 / y_1, \{(0.1, 0.4) / s_1, (0.2, 0.6) / s_2, (0.4, 0.3) / s_3\}), \\ (0.6 / y_4, \{(0.1, 0.5) / s_1, (0.3, 0.5) / s_2, (0.2, 0.7) / s_3\}) \end{array} \right\}$$

then  $\tilde{\tau} = \{G_\emptyset, G_{\bar{R}}, G_U, G_V\}$  is a FPIFS topology on  $R$ . In fact,  $G_V \subseteq G_U$ .

For

- i.  $G_\emptyset, G_{\bar{R}} \in \tilde{\tau}$ ,
- ii.  $G_\emptyset \tilde{\cap} G_U = G_\emptyset, G_\emptyset \tilde{\cap} G_V = G_\emptyset, G_\emptyset \tilde{\cap} G_{\bar{R}} = G_\emptyset,$   
 $G_{\bar{R}} \tilde{\cap} G_U = G_U, G_{\bar{R}} \tilde{\cap} G_V = G_V, G_U \tilde{\cap} G_V = G_V$
- iii.  $G_\emptyset \tilde{\cup} G_U = G_U, G_\emptyset \tilde{\cup} G_V = G_V, G_\emptyset \tilde{\cup} G_{\bar{R}} = G_{\bar{R}},$   
 $G_{\bar{R}} \tilde{\cup} G_U = G_{\bar{R}}, G_{\bar{R}} \tilde{\cup} G_V = G_{\bar{R}}, G_U \tilde{\cup} G_V = G_U$

This implies that  $\tilde{\tau} = \{G_\emptyset, G_{\bar{R}}, G_U, G_V\}$  is a FPIFS topology on  $R$ .

**Definition 2.2** Let  $\tilde{\tau}_1$  and  $\tilde{\tau}_2$  be two FPIFS topologies on  $U$ . If  $\tilde{\tau}_1 \subseteq \tilde{\tau}_2$  then  $\tilde{\tau}_1$  is called FPIFS-courser or FPIFS weaker and  $\tilde{\tau}_2$  is called FPIFS finer or FPIFS stronger than  $\tilde{\tau}_1$ .

**Example 2.3** Let  $R = \{s_1, s_2, s_3\}$  be the set of universe and let  $E = \{y_1, y_2, y_3, y_4\}$  be the set of attributes. If  $U = \{0.2 / y_1, 0.6 / y_2, 0.7 / y_4\} \subseteq E$ ,  $V = \{0.1 / y_1, 0.6 / y_4\}$  with FPIFS sets,

$$G_U = \left\{ \begin{array}{l} (0.2 / y_1, \{(0.2, 0.3) / s_1, (0.3, 0.5) / s_2, (0.8, 0.2) / s_3\}), \\ (0.6 / y_2, \{(0.5, 0.4) / s_1, (0.6, 0.3) / s_2, (0.3, 0.5) / s_3\}), \\ (0.7 / y_4, \{(0.2, 0.4) / s_1, (0.4, 0.4) / s_2, (0.2, 0.6) / s_3\}) \end{array} \right\}$$

and

$$G_V = \left\{ \begin{array}{l} (0.1 / y_1, \{(0.1, 0.4) / s_1, (0.2, 0.6) / s_2, (0.4, 0.3) / s_3\}), \\ (0.6 / y_4, \{(0.1, 0.5) / s_1, (0.3, 0.5) / s_2, (0.2, 0.7) / s_3\}) \end{array} \right\}$$

then  $\tilde{\tau}_1 = \{G_\emptyset, G_{\tilde{R}}, G_U\}$  and  $\tilde{\tau}_2 = \{G_\emptyset, G_{\tilde{R}}, G_U, G_V\}$  are two topologies. It is clear that  $\tilde{\tau}_1 \subseteq \tilde{\tau}_2$ . Thus  $\tilde{\tau}_1$  is called FPIFS-courser or FPIFS-weaker and  $\tilde{\tau}_2$  is called FPIFS-finer or FPIFS-stronger than  $\tilde{\tau}_1$ .

**Theorem 2.1** Let  $(R, \tilde{\tau})$  be a FPIFS topological space and  $\tau^c$  be family of all FPIFS closed sets. Then

- (1)  $G_\emptyset, G_{\tilde{R}} \in \tilde{\tau}'$
- (2) If  $G_U, G_V \in \tilde{\tau}'$  then  $G_U \tilde{\cup} G_V \in \tilde{\tau}'$ ,
- (3) If  $G_{U_i} \in \tilde{\tau}', \forall i \in I$ , then  $\bigcap_{i \in I} G_{U_i} \in \tilde{\tau}'$ .

Proof. Straightforward.

**Remark 2.1**  $\tilde{\tau}_1 \tilde{\cup} \tilde{\tau}_2$  may not be a FPIFS topology on  $R$ . We present an illustration for this with following.

**Example 2.4** Let  $R = \{s_1, s_2, s_3\}$  be the set of universe and let  $E = \{y_1, y_2, y_3, y_4\}$  be the set of attributes. If  $U = \{0.2 / y_1, 0.6 / y_3\} \subseteq E$ ,  $V = \{0.1 / y_2, 0.6 / y_4\} \subseteq E$  with FPIFS sets,

$$G_U = \left\{ \begin{array}{l} (0.2 / y_1, \{(0.2, 0.3) / s_1, (0.3, 0.5) / s_2, (0.8, 0.2) / s_3\}), \\ (0.6 / y_3, \{(0.2, 0.4) / s_1, (0.4, 0.4) / s_2, (0.2, 0.6) / s_3\}) \end{array} \right\}$$

and

$$G_V = \left\{ \begin{array}{l} (0.1 / y_2, \{(0.1, 0.4) / s_1, (0.2, 0.6) / s_2, (0.4, 0.3) / s_3\}), \\ (0.6 / y_4, \{(0.1, 0.5) / s_1, (0.3, 0.5) / s_2, (0.2, 0.7) / s_3\}) \end{array} \right\}$$

then  $\tilde{\tau}_1 = \{G_\emptyset, G_{\tilde{R}}, G_U\}$  and  $\tilde{\tau}_2 = \{G_\emptyset, G_{\tilde{R}}, G_V\}$  are two topologies on  $R$ .

On the other hand, since  $G_U, G_V \in \tilde{\tau}_1 \tilde{\cup} \tilde{\tau}_2$  but  $G_U \tilde{\cup} G_V \notin \tilde{\tau}_1 \tilde{\cup} \tilde{\tau}_2$ ,  $\tilde{\tau}_1 \tilde{\cup} \tilde{\tau}_2 = \{G_\emptyset, G_{\tilde{R}}, G_U, G_V\}$  is not a FPIFS topology on  $R$ . But  $\tilde{\tau}_1 \tilde{\cap} \tilde{\tau}_2 = \{G_\emptyset, G_{\tilde{R}}\}$  is a FPIFS topology on  $R$ .

**Definition 2.3** Let  $(R, \tilde{\tau})$  be a FPIFS topological space and  $G_U \tilde{\subseteq} FPIFS(G_{\tilde{R}})$  then FPIFP-closure of  $G_U$  is written as  $\bar{G}_U$  which is the FPIFS-intersection of all FPIFS-closed supersets of  $G_U$ .

Clearly,  $\bar{G}_U$  is the FPIFP-smallest closed superset of  $G_U$ .

**Theorem 2.2** Let  $(R, \tilde{\tau})$  be a FPIFS topological space and  $G_U, G_V \tilde{\subseteq} FPIFS(G_{\tilde{R}})$ . Then,

1.  $\bar{G}_\emptyset = G_\emptyset$  and  $\bar{G}_{\tilde{R}} = G_{\tilde{R}}$
2.  $G_U \tilde{\subseteq} \bar{G}_U$
3.  $\bar{\bar{G}}_U = \bar{G}_U$
4. If  $G_U \tilde{\subseteq} G_V$ , then  $\bar{G}_U \tilde{\subseteq} \bar{G}_V$
5.  $G_U$  is a FPIFS-closed set if and only if  $G_U = \bar{G}_U$
6.  $\overline{G_U \tilde{\cup} G_V} = \bar{G}_U \tilde{\cup} \bar{G}_V$ .

Proof. The statements (1), (2), (3) and (4) are obvious from the definition of FPIFS closure.

(5) Let  $G_U$  be a FPIFS-closed set. Since  $\overline{G_U}$  is the smallest FPIFS-closed set which contain  $G_U$ , then  $\overline{G_U} \subseteq G_U$ . Therefore, we have  $G_U = \overline{G_U}$ .

(6) Since  $G_U \subseteq G_U \cup G_V$  and  $G_V \subseteq G_U \cup G_V$  by (4),  $\overline{G_U} \subseteq \overline{G_U \cup G_V}$ ,  $\overline{G_V} \subseteq \overline{G_U \cup G_V}$  and hence  $\overline{G_U} \cup \overline{G_V} \subseteq \overline{G_U \cup G_V}$ .

**Definition 2.4** Let  $(R, \tilde{\tau})$  be a FPIFS topological space and  $G_U \subseteq FPIFS(G_{\tilde{R}})$  then FPIFP-interior of  $G_U$  is written as  $G_U^o$  which is the FPIFS-union of all FPIFS-open subset of  $G_U$ .

Clearly,  $G_U^o$  is the FPIFP-largest open set contained in  $G_U$ .

.

**Theorem 2.3** Let  $(R, \tilde{\tau})$  be a FPIFS topological space and  $G_U, G_V \subseteq FPIFS(G_{\tilde{R}})$ . Then,

1.  $G_{\emptyset}^o = G_{\emptyset}$  and  $G_{\tilde{R}}^o = G_{\tilde{R}}$
2.  $G_U^o \subseteq G_U$
3.  $(G_U^o)^o = G_U^o$
4. If  $G_U \subseteq G_V$ , then  $G_U^o \subseteq G_V^o$
5.  $G_U$  is a FPIFS-open set if and only if  $G_U = G_U^o$
6.  $(G_U \cup G_V)^o = G_U^o \cup G_V^o$ .

Proof. It is proved similar to Theorem 2.1.

**Theorem 2.4** Let  $(R, \tilde{\tau})$  be a FPIFS topological space and  $G_U \subseteq FPIFS(G_{\tilde{R}})$ . Then,

1.  $(G_U^o)^c = (\overline{(G_U)^c})$
2.  $\overline{(G_U)^c} = ((G_U^o)^c)$ .

Proof. We only prove (1). The other is similar.

$$\begin{aligned}
 (G_U^o)^c &= (\tilde{\cup}\{G_V : G_V \in \tilde{\tau}, G_U \tilde{\subseteq} G_V\})^c \\
 &= \tilde{\cap}\{(G_V)^c : G_V \in \tilde{\tau}, G_U \tilde{\subseteq} G_V\} \\
 &= \tilde{\cap}\{(G_V)^c : G_V \in \tilde{\tau}', (G_U)^c \tilde{\subseteq} (G_V)^c\} \\
 &= \left(\overline{(G_U)^c}\right)
 \end{aligned}$$

**Definition 2.5** Let  $\tilde{\tau}_1$  be a FPIFS-topology on  $R$  and  $P \subseteq R$  and let  $\tilde{\tau}_2$  be a FPIFS-topology on  $P$  whose FPIFS-open set can be defined as follows;

$$G_V = G_U \tilde{\cap} G_{\tilde{P}}$$

where  $G_U$  is the FPIFS-open sets of  $\tilde{\tau}_1$  and  $G_V$  is the FPIFS-open sets of  $\tilde{\tau}_2$ ,  $G_{\tilde{P}}$  is FPIFS absolute set on  $P$ . Then  $\tilde{\tau}_2$  is known as the FPIFS subspace of  $\tilde{\tau}_1$ .

**Example 2.5** Let  $R = \{r_1, r_2, r_3\}$  be the set of universe and let  $E = \{e_1, e_2, e_3, e_4\}$  be the set of parameters. If  $U = \{0.8/e_1, 0.9/e_3, 0.7/e_4\}$  and  $V = \{0.5/e_1, 0.4/e_4\}$  with the FPIFS sets,

$$G_U = \left\{ \begin{array}{l} (0.8/e_1, \{(0.5, 0.3)/r_1, (0.7, 0.4)/r_2, (0.6, 0.5)/r_3\}), \\ (0.9/e_3, \{(0.4, 0.6)/r_1, (0.3, 0.2)/r_2, (0.4, 0.4)/r_3\}), \\ (0.7/e_4, \{(0.5, 0.2)/r_1, (0.6, 0.3)/r_2, (0.8, 0.1)/r_3\}) \end{array} \right\}$$

and

$$G_V = \left\{ \begin{array}{l} (0.5/e_1, \{(0.5, 0.4)/r_1, (0.2, 0.5)/r_2, (0.3, 0.6)/r_3\}), \\ (0.4/e_4, \{(0.3, 0.3)/r_1, (0.4, 0.5)/r_2, (0.5, 0.2)/r_3\}) \end{array} \right\}$$

then  $\tilde{\tau}_1 = \{G_\emptyset, G_{\tilde{R}}, G_U, G_V\}$  is a FPIFS topology on  $R$ . If  $P = \{r_1, r_2\} \subseteq R$  and  $\Lambda = \{e_1, e_2, e_3, e_4\}$ , then FPIFS absolute set on  $P$  is,

$$G_{\tilde{P}} = \left\{ \begin{array}{l} (1/e_1, \{(1,0)/r_1, (1,0)/r_2\}), \\ (1/e_2, \{(1,0)/r_1, (1,0)/r_2\}), \\ (1/e_3, \{(1,0)/r_1, (1,0)/r_2\}), \\ (1/e_4, \{(1,0)/r_1, (1,0)/r_2\}) \end{array} \right\}$$

where FPIFS open sets for  $\tilde{\tau}_2$  can be calculated as,

$$G_{\tilde{P}} \tilde{\cap} G_\emptyset = G_\emptyset, G_{\tilde{P}} \tilde{\cap} G_{\tilde{R}} = G_\emptyset,$$

$$G_C = G_{\tilde{P}} \tilde{\cap} G_U = \left\{ \begin{array}{l} (0.8/e_1, \{(0.5,0.3)/r_1, (0.7,0.4)/r_2\}), \\ (0.9/e_3, \{(0.4,0.6)/r_1, (0.3,0.2)/r_2\}), \\ (0.7/e_4, \{(0.5,0.2)/r_1, (0.6,0.3)/r_2\}) \end{array} \right\}$$

and

$$G_D = G_{\tilde{P}} \tilde{\cap} G_V = \left\{ \begin{array}{l} (0.5/e_1, \{(0.5,0.4)/r_1, (0.2,0.5)/r_2\}), \\ (0.4/e_4, \{(0.3,0.3)/r_1, (0.4,0.5)/r_2\}) \end{array} \right\}$$

Thus  $\tilde{\tau}_2 = \{G_\emptyset, G_{\tilde{P}}, G_C, G_D\}$  is FPIFS-topology on  $P$ . So  $\tilde{\tau}_2$  is a FPIFS subspace of  $\tilde{\tau}_1$ .

**Remark 2.2 (i)** Every FPIFS-subspace of a discrete FPIFS-topological space is always discrete. Similarly, every subspace of indiscrete FPIFS-topological space is indiscrete.

**(ii)** A subspace  $S$  of a subspace  $P$  of a FPIFS topological space  $R$  is also FPIFS subvspace of  $R$ .

**Remark 2.3** In FPIFS set theory the law of contradiction  $G_U \tilde{\cap} G_U^c = G_\emptyset$  and the law of exluded middle  $G_U \tilde{\cup} G_U^c = G_{\tilde{R}}$  does not hold in general. Then the collection of FPIFS sets  $\{G_\emptyset, G_{\tilde{R}}, G_U, G_U^c\}$  is not a FPIFS-topology on  $R$ .

**Example 2.6** Let  $R = \{r_1, r_2, r_3\}$  be the set of universe and let  $E = \{e_1, e_2, e_3, e_4\}$  be the set of parameters. If  $U = \{0.3/e_1, 0.6/e_2\}$ , then

$$G_U = \left\{ \begin{array}{l} (0.3/e_1, \{(0.6, 0.3)/r_1, (0.5, 0.4)/r_2, (0.2, 0.5)/r_3\}), \\ (0.6/e_2, \{(0.4, 0.5)/r_1, (0.6, 0.3)/r_2, (0.5, 0.5)/r_3\}) \end{array} \right\}$$

and

$$G_U^c = \left\{ \begin{array}{l} (0.7/e_1, \{(0.3, 0.6)/r_1, (0.4, 0.5)/r_2, (0.8, 0.5)/r_3\}), \\ (0.4/e_2, \{(0.5, 0.4)/r_1, (0.4, 0.7)/r_2, (0.5, 0.5)/r_3\}) \end{array} \right\}$$

Clearly,  $\tilde{\tau} = \{G_\emptyset, G_{\bar{R}}, G_U, G_U^c\}$  is not a FPIFS-topology on  $R$ , because  $G_U \tilde{\cap} G_U^c \tilde{\not\subseteq} \tilde{\tau}$  and  $G_U \tilde{\cup} G_U^c \tilde{\not\subseteq} \tilde{\tau}$ .

**Definition 2.6** Let  $G_U$  be a FPIFS-subset of FPIFS topological space  $(R, \tilde{\tau})$ . Then the fronties or boundary of  $G_U$ , denoted as  $Fr(G_U)$  and is defined as,

$$Fr(G_U) = \overline{G_U} \tilde{\cap} \overline{G_U^c}.$$

**Example 2.7** Let  $R = \{r_1, r_2, r_3\}$  be the set of universe and let  $E = \{e_1, e_2, e_3, e_4\}$  be the set of parameters. If  $U = \{0.5/e_1, 0.6/e_2, 0.4/e_3\}$  and  $V = \{0.5/e_1, 0.4/e_4\}$  with the FPIFS sets,

$$G_U = \left\{ \begin{array}{l} (0.5/e_1, \{(0.2, 0.3)/r_1, (0.6, 0.2)/r_2, (0.3, 0.3)/r_3\}), \\ (0.6/e_2, \{(0.5, 0.4)/r_1, (0.7, 0.3)/r_2, (0.8, 0.1)/r_3\}), \\ (0.4/e_3, \{(0.3, 0.3)/r_1, (0.5, 0.2)/r_2, (0.2, 0.2)/r_3\}) \end{array} \right\}$$

$$G_V = \left\{ \begin{array}{l} (0.5/e_1, \{(0.2, 0.4)/r_1, (0.4, 0.3)/r_2, (0.2, 0.3)/r_3\}), \\ (0.4/e_2, \{(0.3, 0.5)/r_1, (0.5, 0.5)/r_2, (0.4, 0.5)/r_3\}) \end{array} \right\}$$

then  $\tilde{\tau} = \{G_\emptyset, G_{\bar{R}}, G_U, G_V\}$  is a FPIFS topology on  $R$ . Thus, the closed sets can be calculated as by taking the complements of FPIFS open sets in  $\tilde{\tau}$ , i.e.,

$$G_{\emptyset}^c = G_{\bar{R}}, G_{\bar{R}}^c = G_{\emptyset},$$

$$G_U^c = \left\{ \begin{array}{l} (0.5/e_1, \{(0.3,0.2)/r_1, (0.2,0.6)/r_2, (0.3,0.3)/r_3\}), \\ (0.4/e_2, \{(0.4,0.5)/r_1, (0.3,0.7)/r_2, (0.1,0.8)/r_3\}), \\ (0.6/e_3, \{(0.3,0.3)/r_1, (0.2,0.5)/r_2, (0.2,0.2)/r_3\}) \end{array} \right\},$$

$$G_V^c = \left\{ \begin{array}{l} (0.5/e_1, \{(0.4,0.2)/r_1, (0.3,0.4)/r_2, (0.3,0.2)/r_3\}), \\ (0.6/e_2, \{(0.5,0.3)/r_1, (0.5,0.5)/r_2, (0.5,0.4)/r_3\}) \end{array} \right\}$$

If  $\Upsilon = \{0.4/e_1, 0.3/e_2, 0.4/e_3\}$ , then FPIFS set on  $R$  is,

$$G_{\Upsilon} = \left\{ \begin{array}{l} (0.4/e_1, \{(0.2,0.4)/r_1, (0.1,0.8)/r_2, (0.3,0.4)/r_3\}), \\ (0.3/e_2, \{(0.3,0.6)/r_1, (0.2,0.7)/r_2, (0.1,0.8)/r_3\}), \\ (0.4/e_3, \{(0.2,0.5)/r_1, (0.1,0.6)/r_2, (0.2,0.4)/r_3\}) \end{array} \right\}$$

This show that FPIFS closed superset of  $G_{\Upsilon}$  are  $G_U^c$  and  $G_{\bar{R}}$  only. Thus  $\overline{G_{\Upsilon}} = G_U^c \tilde{\cap} G_{\bar{R}} = G_U^c$ . On the other hand,

$$G_{\Upsilon}^c = \left\{ \begin{array}{l} (0.6/e_1, \{(0.4,0.2)/r_1, (0.8,0.2)/r_2, (0.4,0.3)/r_3\}), \\ (0.7/e_2, \{(0.6,0.3)/r_1, (0.7,0.2)/r_2, (0.8,0.1)/r_3\}), \\ (0.6/e_3, \{(0.5,0.2)/r_1, (0.6,0.1)/r_2, (0.4,0.2)/r_3\}) \end{array} \right\}$$

So  $\overline{G_{\Upsilon}^c} = G_{\bar{R}}$ . Hence we obtain

$$Fr(G_{\Upsilon}) = \overline{G_{\Upsilon}} \tilde{\cap} \overline{G_{\Upsilon}^c} = G_U^c \tilde{\cap} G_{\bar{R}} = G_U^c.$$

**Definition 2.7** Let  $G_U$  be a FPIFS-subset of FPIFS topological space  $(R, \tilde{\tau})$ . Then the exterior of  $G_U$ , denoted as  $Ext(G_U)$  is defined by  $Ext(G_U) = (\overline{G_U})^c$ .

**Example 2.8** Let  $R = \{r_1, r_2, r_3\}$  be the set of universe and let  $E = \{e_1, e_2, e_3, e_4\}$  be the set of parameters. If  $U = \{0.5/e_1, 0.6/e_2, 0.4/e_3\}$  and  $V = \{0.5/e_1, 0.4/e_4\}$  with the FPIFS sets,

$$G_U = \left\{ \begin{array}{l} (0.5/e_1, \{(0.2, 0.3)/r_1, (0.6, 0.2)/r_2, (0.3, 0.3)/r_3\}), \\ (0.6/e_2, \{(0.5, 0.4)/r_1, (0.7, 0.3)/r_2, (0.8, 0.1)/r_3\}), \\ (0.4/e_3, \{(0.3, 0.3)/r_1, (0.5, 0.2)/r_2, (0.2, 0.2)/r_3\}) \end{array} \right\}$$

$$G_V = \left\{ \begin{array}{l} (0.5/e_1, \{(0.2, 0.4)/r_1, (0.4, 0.3)/r_2, (0.2, 0.3)/r_3\}), \\ (0.4/e_2, \{(0.3, 0.5)/r_1, (0.5, 0.5)/r_2, (0.4, 0.5)/r_3\}) \end{array} \right\}$$

then  $\tilde{\tau} = \{G_\emptyset, G_{\tilde{R}}, G_U, G_V\}$  is a FPIFS topology on  $R$ . Thus, the closed sets can be calculated as by taking the complements of FPIFS open sets in  $\tilde{\tau}$ , i.e,

$$G_\emptyset^c = G_{\tilde{R}}, G_{\tilde{R}}^c = G_\emptyset,$$

$$G_U^c = \left\{ \begin{array}{l} (0.5/e_1, \{(0.3, 0.2)/r_1, (0.2, 0.6)/r_2, (0.3, 0.3)/r_3\}), \\ (0.4/e_2, \{(0.4, 0.5)/r_1, (0.3, 0.7)/r_2, (0.1, 0.8)/r_3\}), \\ (0.6/e_3, \{(0.3, 0.3)/r_1, (0.2, 0.5)/r_2, (0.2, 0.2)/r_3\}) \end{array} \right\},$$

$$G_V^c = \left\{ \begin{array}{l} (0.5/e_1, \{(0.4, 0.2)/r_1, (0.3, 0.4)/r_2, (0.3, 0.2)/r_3\}), \\ (0.6/e_2, \{(0.5, 0.3)/r_1, (0.5, 0.5)/r_2, (0.5, 0.4)/r_3\}) \end{array} \right\}$$

If  $C = \{0.6/e_1, 0.5/e_2\}$ , then FPIFS set on  $R$  is,

$$G_C = \left\{ \begin{array}{l} (0.6/e_1, \{(0.3, 0.3)/r_1, (0.5, 0.2)/r_2, (0.4, 0.1)/r_3\}), \\ (0.5/e_2, \{(0.4, 0.2)/r_1, (0.6, 0.3)/r_2, (0.5, 0.3)/r_3\}) \end{array} \right\}$$

This show that FPIFS open sets contained in  $G_C$  are  $G_V$  and  $G_\emptyset$ . Thus  $G_C^o = G_V \tilde{\cap} G_\emptyset = G_V$ . Thus  $\overline{G_C} = G_{\tilde{R}}$ . So  $Fr(G_C) = \overline{G_C} \tilde{\cap} \overline{G_C^c}$  and thus  $\overline{G_C^c} = G_V^c$ . Hence  $Fr(G_C) = G_{\tilde{R}} \tilde{\cap} G_V^c = G_V^c$ . Therefore  $Ext(G_C) = (\overline{G_C})^c = G_\emptyset$ .

**Theorem 2.5** If  $G_U, G_V, G_Y, G_Z$  are FPIFS sets, then

1.  $G_U^o \neq G_U - (\overline{G_U^c})$
2.  $Ext(G_U^c) = G_U^o$

3.  $Ext(G_U) = (G_U^c)^o$
4.  $Ext(G_U) \tilde{\cup} Fr(G_U) \tilde{\cup} G_U^o \neq G_{\tilde{R}}$
5.  $G_U^o \tilde{\cap} Fr(G_U) \neq G_{\emptyset}$
6.  $\overline{G_U} \neq G_U \tilde{\cup} Fr(G_U)$
7.  $\overline{G_U} \neq G_U^o \tilde{\cup} Fr(G_U)$ .

Proof. By Example-2.4 we observe that  $Ext(G_C) = G_{\emptyset}$ ,  $Fr(G_C) = G_V^c$ ,  $G_C^o = G_V$  and  $\overline{G_C} = G_{\tilde{R}}$ .

1.  $G_U^o \neq G_U - (\overline{G_U^c})$ , because  $G_U - G_V \neq G_U \tilde{\cap} G_V$
2. Clearly,  $Ext(G_U^c) = (\overline{G_U^c})^c$ . Then  $Ext(G_U^c) = [(G_U^c)^c]^o$ . Thus  $Ext(G_U^c) = G_U^o$ .
3. Clearly,  $Ext(G_U) = (\overline{G_U})^o$ . Then  $Ext(G_U) = (G_U^c)^o$ .
4. Clearly,  $Ext(G_U) \tilde{\cup} Fr(G_U) \tilde{\cup} G_U^o \neq G_{\tilde{R}}$ . Then by Example 3.4, we observe that  $G_{\emptyset} \tilde{\cup} G_V^c \tilde{\cup} G_V \neq G_{\tilde{R}}$ .
5. Clearly,  $G_U^o \tilde{\cap} Fr(G_U) \neq G_{\emptyset}$ . Then by Example 3.4, we observe that  $G_U^c \tilde{\cap} G_U \neq G_{\emptyset}$ .
6. It is clear that,  $\overline{G_U} \neq G_U \tilde{\cup} Fr(G_U)$ . By the Example 3.4, we see that  $G_{\tilde{R}} \neq G_Z \tilde{\cup} G_V^c$ .
7. It is clear that,  $\overline{G_U} \neq G_U^o \tilde{\cup} Fr(G_U)$ . By the Example 3.4, we see that  $G_{\tilde{R}} \neq G_V \tilde{\cup} G_V^c$ .

### 3. AN APPLICATION WITH FPIFS TOPOLOGY IN DECISION MAKING

In this section, we proposed a decision-making method using FPIFS topology. It is aimed to select the best components among the options.

**Algorithm-1 for FPIFS set and topology:**

**Input**

**Step-1:** Construct FPIFS sets such that

$$G_U = \left\{ \left( \mu_U(y) / y, \left\{ (\mu(s), \nu(s)) / s \right\} \right) : y \in E, s \in R \right\}.$$

**Step-2:** Construct a FPIFS topology with using proposed FPIFS sets.

**Step-3:** The cardinal of all FPIFS is computed by the formula,

$$cG_U = \{ \mu_{cG_U}(y) / y : y \in E \}$$

where  $\mu_{cG_U}(u) = \sum_{u \in U} \mu_E(y) \cdot (\mu_{G_U^{\omega}}(s)) / |R|$  and

$$\mu_{G_U^{\omega}}(s) = (\mu_{G_U}(s) - \nu_{G_U}(s)).$$

**Step-4:** Obtain the aggregate fuzzy set with using following formula;

$$|E| * M_{G_U^*} = M_{G_U} * M_{cG_U}$$

where  $M_{G_U}, M_{cG_U}, M_{G_U^*}$  are representation matrices of  $G_U, cG_U$  and  $G_U^*$ , respectively.

**Step-5:** Compute final decision set with using following formula

$$\mu_{G_U^* + G_V^*}(s) = \mu_{G_U^*}(s) + \mu_{G_V^*}(s) - [\mu_{G_U^*}(s) * \mu_{G_V^*}(s)]$$

**Output**

**Step-7:** Select the greatest degree of membership by  $\max(\mu_{G_U^* + G_V^*}(s))$ .

**Example 3.1** Let  $R = \{s_1, s_2, s_3, s_4, s_5, s_6, s_7, s_8\}$  be set of alternatives,  $E = \{y_1, y_2, y_3, y_4, y_5, y_6\}$  be a parameter set determined by a decision-maker.

**INPUT:**

**Step-1:** FPIFS sets  $G_U$  and  $G_V$  are the actual results and tabular presentations of the FPIFS sets are given in Table 1 and Table 2, respectively.

$$G_U = \left\{ \begin{array}{l} (0.4/y_1, \{(0.62, 0.31)/s_1, (0.45, 0.48)/s_2, (0.52, 0.34)/s_3, (0.62, 0.23)/s_5\}), \\ (0.3/y_2, \{(0.46, 0.25)/s_2, (0.58, 0.32)/s_3, (0.76, 0.18)/s_4, (0.83, 0.12)/s_7\}), \\ (0.6/y_4, \{(0.74, 0.12)/s_2, (0.56, 0.41)/s_4, (0.63, 0.41)/s_5, (0.38, 0.32)/s_6, (0.57, 0.26)/s_7\}), \\ (0.8/y_6, \{(0.52, 0.15)/s_1, (0.34, 0.24)/s_2, (0.53, 0.36)/s_3, (0.48, 0.32)/s_5, (0.51, 0.24)/s_7, (0.72, 0.23)/s_8\}) \end{array} \right\},$$

$$G_V = \left\{ \begin{array}{l} (0.3/y_1, \{(0.55, 0.36)/s_1, (0.34, 0.49)/s_2, (0.51, 0.42)/s_3, (0.53, 0.28)/s_5\}), \\ (0.4/y_4, \{(0.65, 0.26)/s_2, (0.46, 0.44)/s_5, (0.34, 0.33)/s_6, (0.46, 0.32)/s_7\}), \\ (0.6/y_6, \{(0.43, 0.25)/s_1, (0.21, 0.28)/s_2, (0.38, 0.37)/s_3, (0.61, 0.28)/s_8\}) \end{array} \right\},$$

and

$$G_U^\omega = \left\{ \begin{array}{l} (0.4/y_1, \{0.31/s_1, -0.03/s_2, 0.18/s_3, 0.39/s_5\}), \\ (0.3/y_2, \{0.21/s_2, 0.26/s_3, 0.58/s_4, 0.71/s_7\}), \\ (0.6/y_4, \{0.62/s_2, 0.15/s_4, 0.22/s_5, 0.06/s_6, 0.31/s_7\}), \\ (0.8/y_6, \{0.37/s_1, 0.1/s_2, 0.17/s_3, 0.16/s_5, 0.27/s_7, 0.49/s_8\}) \end{array} \right\},$$

$$G_V^\omega = \left\{ \begin{array}{l} (0.3/y_1, \{0.19/s_1, -0.15/s_2, 0.09/s_3, 0.25/s_5\}), \\ (0.4/y_4, \{0.39/s_2, 0.02/s_5, 0.01/s_6, 0.14/s_7\}), \\ (0.6/y_6, \{0.18/s_1, -0.07/s_2, 0.01/s_3, 0.33/s_8\}) \end{array} \right\},$$

Then.

**Table-1**

$R$	$0.4/y_1$	$0.3/y_2$	$0.6/y_4$	$0.8/y_6$
$s_1$	(0.62, 0.31)	(0,1)	(0,1)	(0.52, 0.15)
$s_2$	(0.45, 0.48)	(0.46, 0.25)	(0.74, 0.12)	(0.34, 0.24)
$s_3$	(0.52, 0.34)	(0.58, 0.32)	(0,1)	(0.53, 0.36)
$s_4$	(0,1)	(0.76, 0.18)	(0.56, 0.41)	(0,1)
$s_5$	(0.62, 0.23)	(0,1)	(0.63, 0.41)	(0.48, 0.32)
$s_6$	(0,1)	(0,1)	(0.38, 0.32)	(0,1)
$s_7$	(0,1)	(0.83, 0.12)	(0.57, 0.26)	(0.51, 0.24)
$s_8$	(0,1)	(0,1)	(0,1)	(0.72, 0.23)

**Table-2**

$U$	$0.3 / y_1$	$0.4 / y_4$	$0.6 / y_6$
$s_1$	(0.55, 0.36)	(0, 1)	(0.43, 0.25)
$s_2$	(0.34, 0.49)	(0.65, 0.26)	(0.21, 0.28)
$s_3$	(0.51, 0.42)	(0, 1)	(0.38, 0.37)
$s_4$	(0, 1)	(0, 1)	(0, 1)
$s_5$	(0.53, 0.28)	(0.46, 0.44)	(0, 1)
$s_6$	(0, 1)	(0.34, 0.33)	(0, 1)
$s_7$	(0, 1)	(0.46, 0.32)	(0, 1)
$s_8$	(0, 1)	(0, 1)	(0.61, 0.28)

**Step 2:** Now we make here a FPFS topology as

$$\tilde{\tau} = \{G_{\emptyset}, G_{\bar{R}}, G_U, G_V\}$$

where  $G_{\emptyset}$  and  $G_{\bar{R}}$  are FPIFS empty and FPIFS absolute sets, respectively.

**Step 3:** The cardinal of all FPIFS is computed by the formula,

$$cG_U = \{\mu_{cG_U}(y) / y : y \in E\}$$

where  $\mu_{cG_U}(u) = \sum_{u \in U} \mu_E(y) \cdot (\mu_{G_U^{\omega}}(s)) / |R|$ . If  $\mu_R(s) - \nu_R(s) \leq 0$ ,

then It is taken as  $\mu_R(s) - \nu_R(s) = 0$ .

Then

$$cG_U = \{0.044 / y_1, 0.66 / y_2, 0.816 / y_4, 1.272 / y_6\}$$

and

$$cG_V = \{0.159 / y_1, 0.224 / y_4, 0.306 / y_6\}$$

The cardinal for  $H_{\emptyset}$  and  $H_{\bar{E}}$  are following as respectively,

$$cG_{\emptyset} = \{0 / y_1, 0 / y_2, 0 / y_3, 0 / y_4, 0 / y_5, 0 / y_6\}$$

$$cG_{\bar{R}} = \{1/y_1, 1/y_2, 1/y_3, 1/y_4, 1/y_5, 1/y_6\}$$

(The null set and absolute set are ignored because they do not contain a comment.)

**Step 4:** We use here this formula to find the aggregate fuzzy set,

$$|E| * M_{G_U^*} = M_{G_U^\omega} * M_{cG_U} \quad (4.1)$$

where  $M_{G_U^\omega}, M_{cG_U}, M_{G_U^*}$  are representation matrices of  $G_U^\omega, cG_U$  and  $G_U^*$ , respectively. Then we find out the matrix of  $G_U^*$  by using (4.1).

$$M_{G_U^*} = \frac{1}{6} \begin{bmatrix} 0.31 & 0 & 0 & 0 & 0 & 0.37 \\ 0 & 0.21 & 0 & 0.62 & 0 & 0.1 \\ 0.18 & 0.26 & 0 & 0 & 0 & 0.17 \\ 0 & 0.58 & 0 & 0.15 & 0 & 0 \\ 0.39 & 0 & 0 & 0.22 & 0 & 0.16 \\ 0 & 0 & 0 & 0.06 & 0 & 0.27 \\ 0 & 0.71 & 0 & 0.31 & 0 & 0 \\ 0 & 0 & 0 & 0 & 0 & 0.49 \end{bmatrix} \begin{bmatrix} 0.044 \\ 0.66 \\ 0 \\ 0.816 \\ 0 \\ 1.272 \end{bmatrix} = \begin{bmatrix} 0.0807 \\ 0.1286 \\ 0.0659 \\ 0.0842 \\ 0.0667 \\ 0.0654 \\ 0.1202 \\ 0.1038 \end{bmatrix}$$

that means,

$$G_U^* = \left\{ 0.0807/s_1, 0.1286/s_2, 0.0659/s_3, 0.0842/s_4, \right. \\ \left. 0.0667/s_5, 0.0654/s_6, 0.1202/s_7, 0.1038/s_8 \right\}$$

Similarly, we can find the aggregate for  $G_V^*$  calculated as;

$$M_{G_V^*} = \frac{1}{6} \begin{bmatrix} 0.19 & 0 & 0 & 0 & 0 & 0.18 \\ 0 & 0 & 0 & 0.39 & 0 & 0 \\ 0.09 & 0 & 0 & 0 & 0 & 0.01 \\ 0 & 0 & 0 & 0 & 0 & 0 \\ 0.25 & 0 & 0 & 0.02 & 0 & 0 \\ 0 & 0 & 0 & 0.01 & 0 & 0 \\ 0 & 0 & 0 & 0.14 & 0 & 0 \\ 0 & 0 & 0 & 0 & 0 & 0.33 \end{bmatrix} \begin{bmatrix} 0.159 \\ 0 \\ 0 \\ 0.224 \\ 0 \\ 0.306 \end{bmatrix} = \begin{bmatrix} 0.0142 \\ 0.0145 \\ 0.0028 \\ 0 \\ 0.0073 \\ 0.0003 \\ 0.0052 \\ 0.0168 \end{bmatrix}$$

that means,

$$G_V^* = \left\{ \begin{array}{l} 0.0142 / s_1, 0.0145 / s_2, 0.0028 / s_3, 0 / s_4, 0.0073 / s_5, \\ 0.0003 / s_6, 0.1202 / s_7, 0.0168 / s_8 \end{array} \right\}$$

**Step 5:** Now we find the final decision set by adding  $G_U^*$  and  $G_V^*$  only because there is no need to add the aggregate fuzzy sets of  $G_\emptyset$  and  $G_{\bar{R}}$ . Then

$$\mu_{G_U^*+G_V^*}(s) = \mu_{G_U^*}(s) + \mu_{G_V^*}(s) - [\mu_{G_U^*}(s) * \mu_{G_V^*}(s)]$$

This shows that;

$$G_U^* + G_V^* = \left\{ \begin{array}{l} 0.0937 / s_1, 0.1412 / s_2, 0.0685 / s_3, 0.0842 / s_4, 0.0735 / s_5, \\ 0.6568 / s_6, 0.1247 / s_7, 0.1188 / s_8 \end{array} \right\}$$

**OUTPUT:**

**Step 6:** In the last, we choose the greatest degree of membership by

$$\max(\mu_{G_U^*+G_V^*}(s)) = 0.6568$$

It shows that the  $s_6$  has the greatest membership degree. So,  $s_6$  may be selected between other components.

## **CONCLUSION**

In the present paper, with examples, we define FPFS-topology. We show an unusual use of FPFS-topology to decision-making using various algorithms. To improve the results, we modified various techniques that will be useful to scholars working on IFS-set, FPIFS-set theory, and FPIFS-topology. We expect that the results studied in this study represent a substantial and technically solid addition to the field of FPIFS-set theory.

## REFERENCES

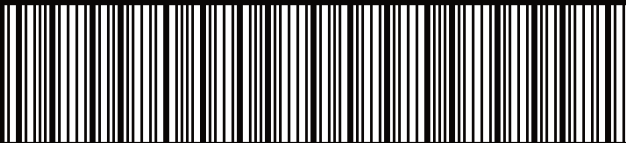
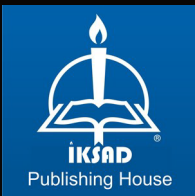
- Acar, U., Koyuncu, F., & Tanay, B. (2010). Soft sets and soft rings. *Computers & Mathematics with Applications*, 59(11), 3458-3463.
- Aktaş, H., & Çağman, N. (2007). Soft sets and soft groups. *Information sciences*, 177(13), 2726-2735.
- Atanassov, K. T. (1986). Intuitionistic fuzzy sets. *Fuzzy Sets and Systems*, 20(1), 87-96.
- Atmaca, S., & Zorlutuna, I. (2013). On fuzzy soft topological spaces. *Ann. Fuzzy Math. Inform*, 5(2), 377-386.
- Aygünoğlu, A., & Aygün, H. (2009). Introduction to fuzzy soft groups. *Computers & Mathematics with Applications*, 58(6), 1279-1286.
- Chang, C. L. (1968). Fuzzy topological spaces. *Journal of mathematical Analysis and Applications*, 24(1), 182-190.
- Çağman, N., Çıtak, F., & Enginoğlu, S. (2010). Fuzzy parameterized fuzzy soft set theory and its applications. *Turkish Journal of Fuzzy Systems*, 1(1), 21-35.
- Çağman, N., Karataş, S., & Enginoglu, S. (2011). Soft topology. *Computers & Mathematics with Applications*, 62(1), 351-358.
- Çağman, N., & Deli, I. (2012). Means of FP-soft sets and their applications. *Hacettepe Journal of Mathematics and Statistics*, 41(5), 615-625.
- Çagman, N., & Enginoglu, S. (2011). FP-soft set theory and its applications. *Ann. Fuzzy Math. Inform*, 2(2), 219-226.
- Çağman, N., & Enginoğlu, S. (2010). Soft set theory and uni-int decision making. *European journal of operational research*, 207(2), 848-855.
- Celik, Y., & Ekiz, C. (2011). A New View on Soft Rings ABSTRACT| FULL TEXT. *Hacettepe Journal of Mathematics and Statistics*, 40(2), 273-286.
- Chen, D., Tsang, E. C. C., Yeung, D. S., & Wang, X. (2005). The parameterization reduction of soft sets and its

- applications. *Computers & Mathematics with Applications*, 49(5-6), 757-763.
- Feng, F., Jun, Y. B., Liu, X., & Li, L. (2010). An adjustable approach to fuzzy soft set based decision making. *Journal of Computational and Applied Mathematics*, 234(1), 10-20.
- İnan, E., & Öztürk, M. A. (2012). Fuzzy soft rings and fuzzy soft ideals. *Neural Computing and Applications*, 21(1), 1-8.
- Kong, Z., Gao, L., & Wang, L. (2009). Comment on “A fuzzy soft set theoretic approach to decision making problems”. *Journal of computational and applied mathematics*, 223(2), 540-542.
- Maji, P. K., Roy, A. R., & Biswas, R. (2002). An application of soft sets in a decision making problem. *Computers & Mathematics with Applications*, 44(8-9), 1077-1083.
- Maji, P. K., Biswas, R. and Roy, A. R. (2001). *Fuzzy soft sets*, Journal of Fuzzy Mathematics, 203 (2), 589-602.
- Molodtsov, D. (1999). *Soft set theory-First results*, Comput. Math. Appl. 37 (4/5), 19-31.
- Riaz, M. and Hashmi, M.R. (2017). Fuzzy parameterized fuzzy soft topology with applications, Ann. Fuzzy Math. Inform. 13(5), 593-613.
- Roy, A.R. and Maji, P.K. (2007). *A fuzzy soft set theoretic approach to decision making problems*, J. Comput. Appl. Math. 203, 412-418.
- Shabir, M. and Naz, M. (2011). *On soft topological spaces*, Comput. Math. Appl. 61, 1786-1799.
- Simsekler, T. and Yuksel, S. (2013). *Fuzzy soft topological spaces*, Ann. Fuzzy Math. Inform. 5 (1), 87-96, 2013.
- Sulukan, E. , Cagman, N. & Aydın, T. (2019). Fuzzy Parameterized Intuitionistic Fuzzy Soft Sets and Their Application to a Performance-Based Value Assignment Problem. *Journal of New Theory* , (29) , 79-88
- Zadeh, L. A. (1965). *Fuzzy sets*, Inform. and Control 8, 338-353.
- Zhan J, Liu Q, Davvaz B (2015) A new rough set theory: rough soft hemirings. *J Intell Fuzzy Syst* 28:1687–1697

Zorlutuna, 'I., Akdag, M., Min,W. K. and Atmaca, S. (2011). *Remarks on soft topological spaces*, Ann. Fuzzy Math. Inform. 3 (2), 171-185.

Zorlutuna I. And Atmaca, S. (2016). Fuzzy parametrized fuzzy soft topology, New Trends in Mathematical Sciences 4 (1), 142-152.





**ISBN: 978-625-8213-11-9**